coatings

Review

Recent Advances in the Performance and Mechanisms of High-Entropy Alloys Under Low- and High-Temperature Conditions

Rui Xi [1] and Yanzhou Li [2,*]

[1] School of Mechanical Engineering, North China University of Water Resources and Electric Power, Zhengzhou 450045, China; xirui@ncwu.edu.cn
[2] School of Mechanical and Vehicle Engineering, West Anhui University, Lu'an 237010, China
* Correspondence: liyanzhou9336@163.com; Tel.: +86-150-4421-1299

Abstract: High-entropy alloys, since their development, have demonstrated great potential for applications in extreme temperatures. This article reviews recent progress in their mechanical performance, microstructural evolution, and deformation mechanisms at low and high temperatures. Under low-temperature conditions, the focus is on alloys with face-centered cubic, body-centered cubic, and multi-phase structures. Special attention is given to their strength, toughness, strain-hardening capacity, and plastic-toughening mechanisms in cold environments. The key roles of lattice distortion, nanoscale twin formation, and deformation-induced martensitic transformation in enhancing low-temperature performance are highlighted. Dynamic mechanical behavior, microstructural evolution, and deformation characteristics at various strain rates under cold conditions are also summarized. Research progress on transition metal-based and refractory high-entropy alloys is reviewed for high-temperature environments, emphasizing their thermal stability, oxidation resistance, and frictional properties. The discussion reveals the importance of precipitation strengthening and multi-phase microstructure design in improving high-temperature strength and elasticity. Advanced fabrication methods, including additive manufacturing and high-pressure torsion, are examined to optimize microstructures and improve service performance. Finally, this review suggests that future research should focus on understanding low-temperature toughening mechanisms and enhancing high-temperature creep resistance. Further work on cost-effective alloy design, dynamic mechanical behavior exploration, and innovative fabrication methods will be essential. These efforts will help meet engineering demands in extreme environments.

Keywords: high-entropy alloys; low-temperature performance; high-temperature performance; strengthening mechanisms

Academic Editor: Hideyuki Murakami

Received: 9 December 2024
Revised: 11 January 2025
Accepted: 13 January 2025
Published: 15 January 2025

Citation: Xi, R.; Li, Y. Recent Advances in the Performance and Mechanisms of High-Entropy Alloys Under Low- and High-Temperature Conditions. *Coatings* **2025**, *15*, 92. https://doi.org/10.3390/coatings15010092

1. Introduction

As science and technology advance swiftly, the application settings in critical areas like aerospace, energy, transportation, and defense are growing more intricate. Taking the aerospace industry as an example, with the continuous increase in engine operating temperatures, they have approached or even exceeded the melting points of traditional high-temperature alloys, creating an urgent need for structural materials with higher thermal resistance [1–8]. Applications like deep space, deep sea exploration, and superconductivity demand materials capable of maintaining strength and toughness under low and ultra-low temperature conditions to endure extreme environments [9–17]. Simultaneously, in new

application areas such as space debris mitigation and fusion reactors, service conditions involving high loads and variable temperatures require enhanced mechanical properties of materials over extensive temperature spans [18–25]. These application requirements necessitate materials that exhibit excellent physical properties under extreme temperature conditions and maintain good mechanical performance and long-term stability.

Beyond bulk materials, coatings have also been the focus of numerous studies for their role in enhancing material performance under such extreme conditions. Advanced coatings, including ceramic and metallic coatings, show potential to improve oxidation resistance, thermal insulation, and wear resistance of substrate materials at high temperatures [26–28]. For instance, thermal barrier coatings are widely used in aero-engines to protect superalloys from thermal degradation and extend their service life [29–31]. Similarly, low-temperature applications require coatings that can mitigate embrittlement, reduce friction, and enhance surface durability, ensuring long-term stability in cryogenic environments [32,33].

However, the impact of temperature changes on materials is highly complex. At low temperatures, the plasticity and toughness of alloys typically decrease significantly, dislocation movement becomes more difficult, and alloys are more prone to brittle failure [34–45]. At high temperatures, alloys may experience issues such as grain coarsening, phase transitions, creep, and oxidation, leading to decreased material strength, reduced flexibility, and an increased risk of fatigue and fracture [46–54].

Within this framework, the idea of multi-principal-element high-entropy alloys (HEAs), proposed and developed over the past two decades, has provided new ideas for material design in extreme application environments [55–67]. Researchers have found that a multi-element mixture strategy can create complex and diverse microstructures, synergistically activating multiple strengthening mechanisms to enhance the material's overall performance [68–80]. HEAs have shown extensive application possibilities in harsh environments, including extremely low and high temperatures, broad temperature fluctuations, high-velocity impacts, radiation-induced damage, and cyclic loading [81–85].

This paper will review the latest research advancements and theoretical progress on HEAs fabricated using various methods under low and ultra-high temperature conditions. The common microstructure types of HEAs and their deformation mechanisms under extreme loading environments will be discussed, along with important unresolved research issues, and the paper will conclude with an outlook on future research directions.

2. Introduction and Structural Characteristics of HEAs

2.1. Introduction to HEAs

In 2004, Cantor et al. and Yeh et al. introduced HEAs as a novel category of metallic materials that question conventional alloy design principles [86,87]. Conventional alloys usually contain one or two main components, supplemented by other elements to enhance their characteristics. Conversely, HEAs incorporate four or more constituents in approximately equal atomic proportions, resulting in a straightforward lattice structure with extensive chemical randomness. Typically, these alloys develop as a single-phase solid solution. Including numerous primary elements in HEAs inhibits the development of intermetallic compounds (IC). By suppressing IC formation, HEAs address the key limitations found in conventional alloy systems, offering enhanced design flexibility. The discovery of HEAs has disrupted the conventional understanding of phase behaviors in metals and significantly expanded the scope for alloy composition design.

Figure 1 illustrates the development history of HEAs [88–90]. Initial studies primarily examined the architecture and fundamental characteristics of HEAs. With the expansion of industrial requirements, additional functional attributes—including resistance to radiation and corrosion, hydrogen storage capabilities, and catalytic efficiency—started to garner

interest [91–102]. Further research discovered that HEAs exhibit excellent mechanical properties under low and high-temperature conditions. This has led to significant advances in traditional applications and broadened their potential in extreme temperature environments such as low and high temperatures, driving their widespread prospects in engineering.

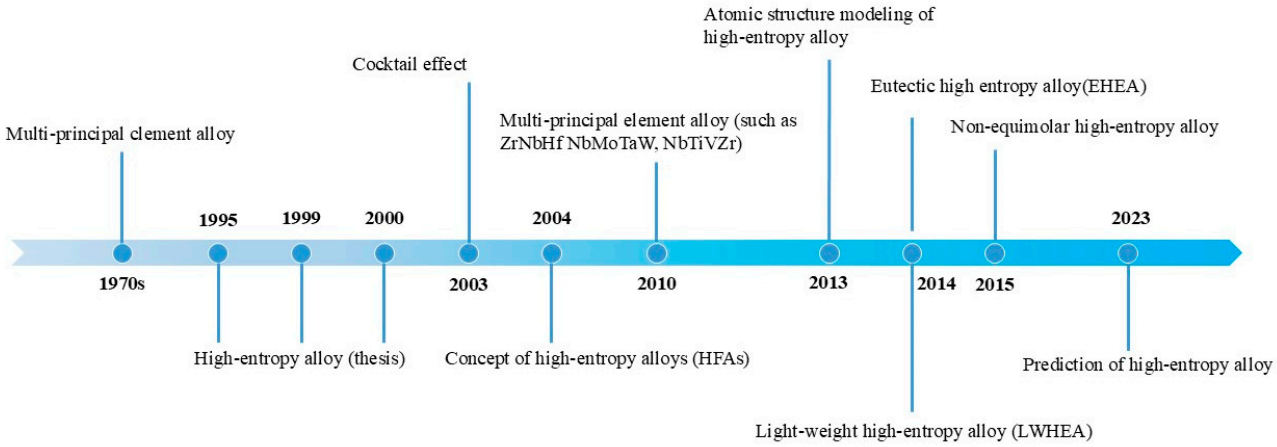

Figure 1. Overview of the historical evolution and milestones in HEA research.

2.2. Chemical Disorder Structure of HEAs

HEAs comprise multiple primary elements, and their phase structure governs the material properties. Entropy is a major factor affecting the structure and a measure of the system's stability. The thermodynamic mixing entropy refers to the configurational entropy of the system. Elevated mixing entropy decreases the phase count in HEAs relative to that anticipated by Gibbs' phase rule, thereby improving the interaction among the primary constituents [90]. As stated by the Gibbs free energy equation ($\Delta G_{mixed} = \Delta H_{mixed} - T\Delta S_{mixed}$, here, ΔG_{mixed} represents the alloy system's free energy, ΔH_{mixed} denotes the mixing enthalpy, ΔS_{mixed} signifies the mixing entropy, and T stands for the temperature), higher mixing entropy helps lower the system's free energy, maintaining the solid solution framework and inhibiting the creation of IC. As a result, HEAs preserve a consistent solid solution architecture at elevated temperatures and display chemical randomness traits, as shown in Figure 2 [90].

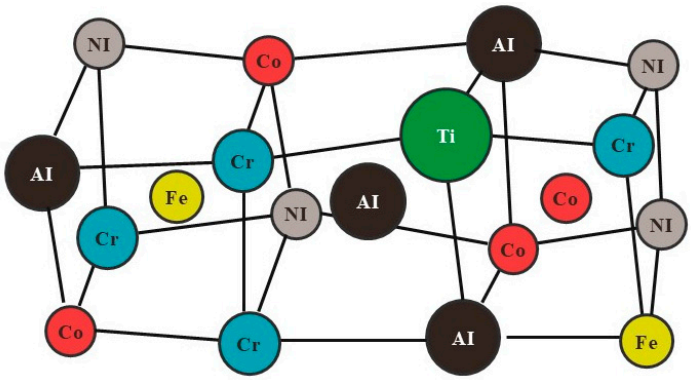

Figure 2. Schematic diagram of lattice distortion in HEAs [90].

The development of solid solution phases is additionally affected by elements like atomic size disparity (δ), electronegativity difference, and mixing enthalpy among the major elements. When $\delta \leq 6.6\%$, reduced lattice distortions promote the establishment of solid solutions [103–107]. Valence electron concentration (VEC) serves as a predictor for de-

termining the crystal structure of HEAs. For VEC values exceeding eight, an FCC structure is probable [108–110]. The majority of HEAs generally develop crystalline architectures, where the FCC structure offers excellent plasticity yet lower strength. Conversely, the BCC structure provides enhanced strength but increased brittleness [111–113]. Due to the slower atomic diffusion kinetics in HEAs, they may also form amorphous or nanocrystalline phases [114–116].

Furthermore, Luan et al. [117] highlighted that adding more elements directly amplifies the number of potential IC within the alloy matrix. The impact of mixing enthalpy on low-temperature environments becomes more significant, and the formation of IC reduces the system's free energy. As a result, most HEAs tend to form multi-phase structures. The combined influence of various factors makes the phase formation behavior of HEAs highly complex, offering extensive opportunities for controlling their microstructural characteristics. This complexity also provides a broad space for designing and optimizing HEAs with tailored properties.

Recent research has confirmed that alloys with non-equal atomic ratios can maintain a stable solid solution structure and that variations in specific elements can notably impact their properties [118,119]. This "cocktail effect" enables HEAs to retain phase stability across a broader range of compositions, which expands their potential for applications in challenging and extreme environments [120,121].

Additionally, studies have revealed that HEAs often display elemental segregation, as seen in ordered oxygen complexes in TiZrNbHf alloys and other ordered phases in similar materials [122–124]. These nanoscale-ordered structures challenge the traditional concept of chemical disorder in HEAs, offering a new understanding of solid material deformation mechanisms. This creates new opportunities for developing stronger and tougher alloys, with important scientific implications.

3. Low-Temperature Properties of HEAs

In their 2011 study on the low-temperature performance of HEAs, Qiao et al. [125] were the pioneers in examining the behavior of the AlCoCrFeNi HEA, which possesses a single-phase BCC structure. They found that this alloy exhibited exceptional compressive performance at low temperatures, with a yield strength reaching 1.88 GPa, and displayed serrated flow behavior. In 2013, a research team led by George E.P. [126] from Oak Ridge National Laboratory investigated the low-temperature properties of CoCrFeNiMn and CoCrFeNi alloys (later known as Cantor alloys), revealing that both strength and ductility markedly enhanced with decreasing temperatures. Specifically, the tensile strength (TS) of the CoCrFeNi HEA surpassed 1 GPa at 77 K, with an elongation greater than 60%. As research on HEAs has advanced, the scope has expanded beyond the low-temperature tensile and compressive performance of equimolar HEAs. For example, studies on non-equimolar HEAs at low temperatures, such as $AlCoCrFeNi_{2.1}$ [127,128], $CrMnFeCoNi_2Cu$ [129], and $Al_{0.5}CoCrCuFeNi$ [130,131], have been increasingly performed. Furthermore, research has also covered various aspects of HEAs under low-temperature conditions, including elastic properties, corrosion resistance, and electromagnetic behaviors. This chapter will provide a classified review of the research developments based on the lattice structures of HEAs.

3.1. FCC-Phase HEAs

3.1.1. CoCrFeMnNi HEA

Recent research into the plastic deformation of HEAs has shown that, in comparison to traditional materials, certain FCC-phase HEAs exhibit a unique characteristic of "increasing strength and toughness at lower temperatures". CoCrFeMnNi, a widely studied single-phase FCC HEA, was one of the earliest alloys investigated for its low-temperature

mechanical properties. As mentioned earlier [126], it was found that the tensile strength(TS) and flexibility of CoCrFeMnNi improved significantly at 77 K. Building upon this, in study [132], the impact of grain size on the low-temperature mechanical characteristics and deformation mechanisms of HEAs was further investigated. FCC HEAs undergo the formation of nanotwins during the later stages of low-temperature deformation, where the abundance of low-energy interfaces generated by twinning refines the grains. These low-energy interfaces effectively hinder dislocation motion, increasing the material's work-hardening rate and delaying necking behavior. The simultaneous effects of dislocation slip and twinning mechanisms significantly boosted the strength and ductility of Cantor alloys at 77 K.

Building upon earlier findings, later research has uncovered how nanotwinning contributes to the improvement in low-temperature mechanical properties in HEAs. The Ritchie research team from the University of California, Berkeley, reported in 2014 that [133] CrMnFeCoNi alloys exhibited excellent fracture toughness at liquid nitrogen temperatures, confirming that the formation of numerous nanotwins was the microstructural origin of their superior low-temperature mechanical performance. The appearance of nanotwins refined the grains, and the abundance of low-energy interfaces further improved the mechanical properties at low temperatures. The research also found that the lower stacking fault energy in HEAs leads to twinning deformation characteristics, where dislocation motion is hindered at low temperatures, and the synergistic effect of twinning and dislocations enables HEAs to exhibit the "stronger and tougher at lower temperatures" behavior [133,134]. In 2014, Gludovatz et al. [133] evaluated the fracture toughness of single-phase FCC HEAs at both ambient and low temperatures. Their findings revealed that the alloy exhibited exceptional toughness at low temperatures, achieving fracture toughness values above 200 MPa·$m^{1/2}$ during crack initiation and exceeding 300 MPa·$m^{1/2}$ during crack propagation at 77 K.

A study on the CoCrFeMnNi HEA examined its mechanical properties under multidirectional loading across temperatures ranging from 113 K to 1273 K, emphasizing its performance under directional stress. Kim et al. [135] found that although the alloy had a strong <111> or <001> crystallographic texture, the elongation to fracture (Ef) was affected by the loading direction. Concurrently, both yield strength (TS) and toughness exhibited minimal dependence on the direction of loading. Figure 3 depicts the correlations among tensile YS, TS, and elongation to fracture (Ef) as they relate to temperature and loading direction. YS and TS were highest at 113 K, indicating excellent strength at low temperatures, with the loading direction having minimal impact on these properties. At 773 K, the as-cast alloy showed the highest Ef, offering better flexibility than the wrought alloy at 673 K. However, above 973 K, Ef decreased sharply, signaling reduced ductility at elevated temperatures.

V-notch Charpy impact test results indicated that, between −150 °C and 150 °C, the as-cast HEA absorbed about half the impact energy compared to the wrought alloy. Despite the reduced absorbed energy, the as-cast alloy did not demonstrate considerable temperature dependence or low-temperature embrittlement. Along different loading directions, the WL direction showed the highest absorbed impact energy, while the WS and H directions were relatively lower, indicating a degree of anisotropy. However, overall, the anisotropy observed in both tensile and impact tests was insignificant. Moreover, under reduced temperatures, the as-cast alloy's impact toughness exceeded that of numerous conventional alloys, displaying strong embrittlement resistance.

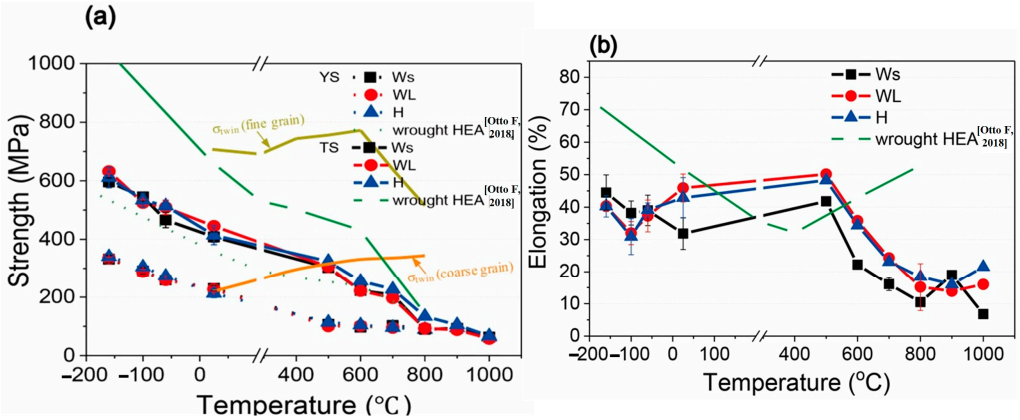

Figure 3. Variations in (**a**) mechanical strength and (**b**) fracture strain across temperatures ranging from 113 K to 1273 K and different loading directions [135].

Analysis of strain hardening behavior indicated that the as-cast HEA underwent three discernible stages across 113 K, ambient temperature 298 K, 773 K, and 973 K. In Stage I, the hardening rate declined; in Stage II, it rose owing to deformation twin formation; and in Stage III, it dropped again following twin saturation. Notably, at 773 K, twin formation was highly active, contributing to the improved flexibility at this temperature. At 700 °C, however, only a limited quantity of twin boundaries was detected, and the number of recrystallized grains increased, as the deformation mechanism transitioned from planar to wavy slip, a marked reduction in flexibility ensued. This indicates that twin activity was greatly suppressed at high temperatures, with recrystallization and dislocation slip becoming the dominant deformation mechanisms.

Further investigations have highlighted twinning's contribution to improving HEA properties at low temperatures. For example, Kireeva et al. [136] examined the deformation behavior of CoCrFeMnNi HEA single crystals. Their findings indicate that at 296 K, the [137]-oriented crystal primarily deforms via dislocation slip up to 30% strain, after which twinning appears. In contrast, the [123]- and [011]-oriented crystals deform predominantly through dislocation slip until failure. At 77 K, twinning becomes the primary deformation mechanism. In the [137]-oriented crystal, deformation transitions to twinning after a 5% slip, while in the [111]-oriented crystal, twinning initiates after a 20% slip. The strain hardening rate decreased in tandem, as shown in Figure 4. At 77 K and 20% strain, [111]-oriented crystals displayed dense dislocations alongside intersecting twins with around 15–20 nm thicknesses. By 35% strain, twinning predominantly takes place in a single system, and after treatment, twins are not visible on the surface, indicating they are very thin and uniformly distributed throughout the crystal. Compared to RT(RT), the alloy exhibits significantly improved flexibility and plasticity at 77 K, highlighting the crucial role of twinning in enhancing the toughness and strength of the HEA at low temperatures.

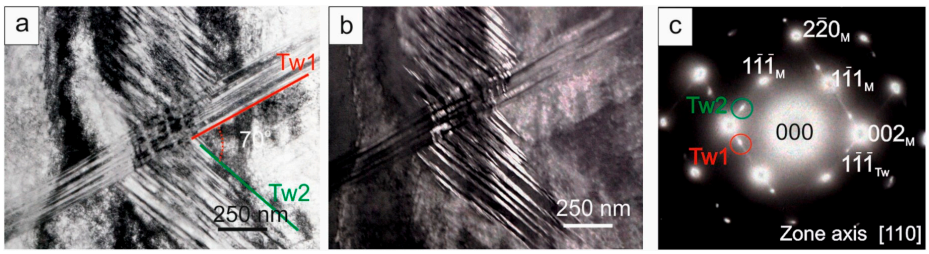

Figure 4. Twin interactions in [111]-oriented CoCrFeMnNi HEA crystals subjected to 20% tensile deformation at 77 K are shown as: (**a**) a bright-field image, (**b**) a dark-field image, and (**c**) a diffraction pattern [136].

In addition to these findings, Rusakova et al. [138] compared the mechanical properties of initial coarse-grained samples and nanocrystalline variants before and after high-pressure torsion (HPT) at low temperatures in CoCrFeNiMn HEAs. The as-cast CoCrFeNiMn HEA was annealed and rolled to achieve an average grain size of four microns. Following HPT treatment at RT, the grain size diminished to 40–80 nm, yielding a uniform microstructure, and only a few grains exceeded 200 nm. Low-temperature HPT treatment resulted in a more heterogeneous structure, with nanocrystalline grains and larger grains up to 500 nm in size. Within the examined temperature interval (77 K to 290 K), microhardness increased as the temperature decreased, indicating that thermally activated processes significantly influenced the plastic deformation mechanism of the material at low temperatures. For the cryo-HPT-treated sample, the variation in microhardness along the disk diameter showed distinct differences. The microhardness rose approximately 35%–40% as it extended from the sample's center to a radius of 1.5–2 mm, increasing from 3 GPa up to 4.25 GPa. In the RT-HPT-treated specimen, microhardness elevated from 3.5 GPa to 4.75 GPa, following a comparable trend, although the cryo-HPT-induced microhardness increase was less pronounced. Microhardness surged from an initial 1.4 GPa to 4.25 GPa with cryo-HPT treatment and to 4.75 GPa following RT-HPT processing. In all studied temperature ranges from 77 K to 290 K, microhardness increased as the temperature decreased, indicating that thermally activated processes substantially governed the material's plastic deformation mechanisms under low-temperature conditions.

3.1.2. Equimolar CoCrFe-Based HEAs

While CoCrFeMnNi remains the most extensively studied FCC phase HEA for low-temperature applications, research has expanded to include other equimolar FCC phase HEAs, exploring their low-temperature behaviors. Tan et al. [139] investigated lattice distortions, the evolution of magnetic properties, and associated behaviors in CrCoNi, CrFeCoNi, and CrMnFeCoNi HEA across various temperatures. As decreasing temperatures, the lattice parameters of each alloy significantly contracted. The lattice contraction for CrCoNi MEA was 1.425%, for CrFeCoNi HEA, 2.278%, and for CrMnFeCoNi HEA, it was the greatest, at 3.476%. As the temperature dropped from 293 K to 123 K, the local lattice distortions in each of the three alloys generally diminished. CrFeCoNi HEA showed the most dramatic changes, especially below 173 K, where changes in the local structure were observed. In terms of magnetism, the CrFeCoNi HEA shifted from a paramagnetic to a ferromagnetic state near 34 K and retained its ferromagnetic properties at 25 K and 5 K, exhibiting soft magnetic behavior. Throughout the entire low-temperature spectrum (77 K, 25 K, and 5 K), both CrCoNi MEA and CrMnFeCoNi HEA stayed paramagnetic, exhibiting only minor increases in magnetization. At low temperatures, the stress–strain profiles for all three alloys displayed comparable serrated patterns, suggesting analogous deformation mechanisms. As the temperature declined from 293 K to 123 K and down to 5 K, the lattice distortions in all three alloys underwent substantial alterations. Additionally, the CrFeCoNi HEA experienced a notable magnetic transition below 173 K, shifting from paramagnetic to ferromagnetic. In contrast, CrCoNi MEA and CrMnFeCoNi HEA did not undergo such a transition.

The impact of alloying elements such as Cu on the magnetic properties at low temperatures has also been explored. Chaudhary et al. [140] examined how adding copper affects the low-temperature magnetic properties of FeCoNiCrCu HEA. At RT, the FeCoNiCr alloy maintains a single-phase FCC. The alloy exhibits paramagnetic behavior with a Curie temperature of 85 K. As the copper content rises from 0 to 0.5, Ms increases from 30.7 emu/g to 32.7 emu/g. However, the XRD patterns reveal the presence of two FCC phases, one of which is enriched with copper. The copper-rich regions primarily appear as small clusters,

ranging from 3 to 5 nm in size, and these clusters are distributed within the FCC matrix, forming a copper-enriched nanostructure.

At low temperatures, the saturation magnetization of FeCoNiCrCux alloys shows a noticeable enhancement. When the copper content increases from 0 to 0.5, Ms increases from 30.7 emu/g to 32.7 emu/g. This increase in saturation magnetization indicates that the addition of copper significantly enhances the low-temperature magnetism of the alloy. The improved magnetic properties suggest that copper affects the alloy's microstructure and strengthens the magnetic exchange interactions within the alloy, thereby enhancing its magnetic performance. Figure 5 shows Cu's distribution and structural characteristics in the FeCoNiCrCu0.5 alloy. Figure 5a displays the individual ion distributions of Fe, Co, and Cu, illustrating that copper forms nanoscale clusters within the FCC matrix, each approximately 3 to 5 nm in size. Figure 5b analyzes the composition variation between the fcc matrix and Cu clusters using a proximity histogram, revealing that the Cu clusters comprise around 92% Cu and 5% Ni, along with approximately 1% Fe, Co, and Cr. Figure 5c displays the morphology of Cu clusters of different sizes obtained through atom probe tomography reconstruction, and further 1-D compositional analysis indicates that the cluster size influences its composition, with larger Cu clusters containing a higher Cu content.

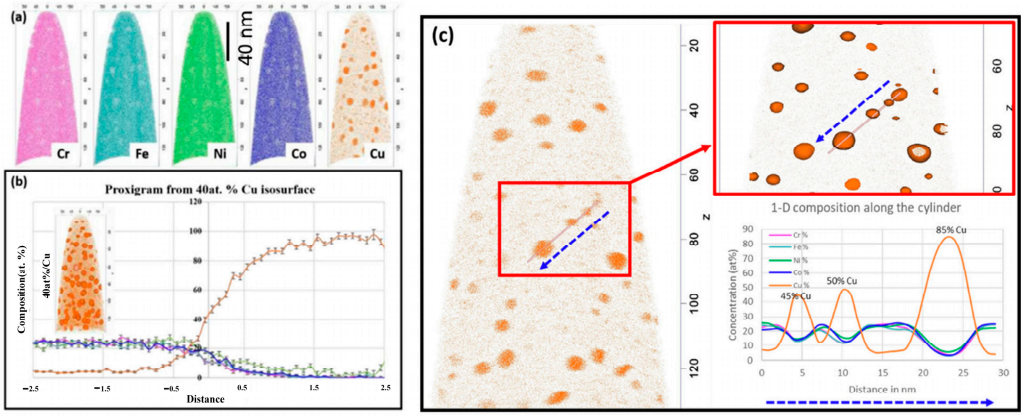

Figure 5. (**a**) Elemental distributions of Cr, Fe, Ni, Co, and Cu in the FeNiCoCrCu0.5 HEA; (**b**) Composition variations between the FCC matrix and Cu-rich areas; (**c**) atom probe tomography reconstruction illustrating Cu distribution, enlarged cluster images, and a one-dimensional composition analysis [140].

3.1.3. Non-Equimolar HEAs

Building on the understanding gained from equimolar HEAs, researchers have explored non-equimolar HEAs by adjusting alloying element ratios to develop compositions with improved low-temperature performance. Tabachnikova et al. [129] explored the mechanical properties and fracture behaviors of $CrMnFeCoNi_2Cu$ alloys under low-temperature conditions. The $CrMnFeCoNi_2Cu$ alloy has an FCC crystal structure, and in state II, after 60% rolling deformation, the alloy exhibits a bimodal FCC structure. Compression and tensile tests were conducted in the 300 K to 4.2 K temperature range. The results showed that the alloy exhibits high plasticity under compression, especially at low temperatures below 15 K, where it displays jump-like plastic flow. Under compression, the jump depth $\Delta\tau$ is approximately 44 MPa initially. As the strain progresses from 1% to 2%, the jump depth escalates to around 115 MPa. During tensile deformation, the alloy forms a necking phenomenon, and fracture occurs along a plane at approximately 45° to the tensile axis. Even at low temperatures of 4.2 K, the alloy maintains ductile fracture characteristics.

Figure 6 depicts the tensile fracture surface morphology of the $CrMnFeCoNi_2Cu$ alloy across various temperatures, from 300 K to 4.2 K. At 300 K, the alloy displays standard ductile fracture features, including numerous flat areas and elongated protrusions on the fracture surface. As the temperature decreases to 200 K and 100 K, the fracture surface maintains ductile features but with more pronounced plastic deformation traces, and the size and shape of the protrusions change. Upon further lowering the temperature to 50 K, while ductile features are still present, the brittle component increases, and more microcracks appear on the fracture surface. High magnification images show that at 100 K and 4.2 K, local inhomogeneities and microcracks become more noticeable, indicating that slip localization and microcrack formation are more active at lower temperatures. Remarkably, even at an ultralow temperature of 4.2 K, the alloy maintains ductile fracture traits, showcasing evident plastic deformation and protrusions on the fracture surface. This indicates that the alloy retains substantial plasticity and toughness under low-temperature conditions. In general, decreasing temperatures lead to a gradual reduction in the alloy's ductility and an increase in its brittleness. Nevertheless, the alloy continues to exhibit considerable plastic deformation capacity even at low temperatures.

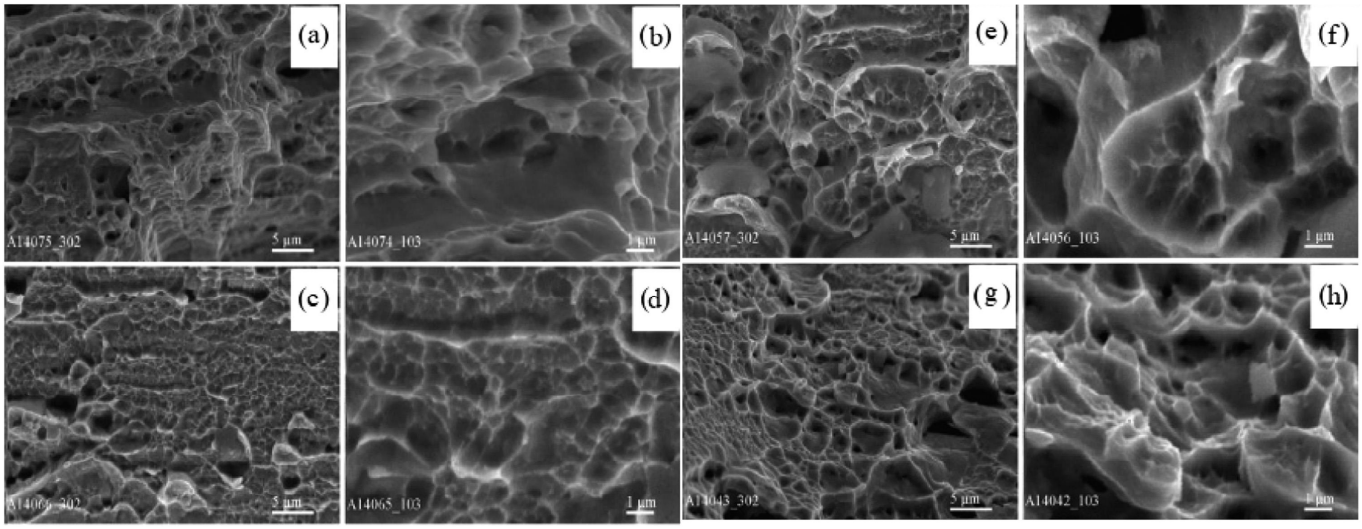

Figure 6. Fracture surface morphology of $CrMnFeCoNi_2Cu$ alloy under tensile deformation at various temperatures. (**a**) 300 K. (**b**) Partial enlarged view of (**a**). (**c**) 77 K. (**d**) Partial enlarged view of (**c**). (**e**) 10 K. (**f**) Partial enlarged view of (**e**). (**g**) 4.2 K. (**h**) Partial enlarged view of (**g**) [129].

Investigating the combined effects of low temperatures and high strain rates is essential for comprehending the mechanical boundaries of HEAs. Jiang et al. [141] examined $Cr_{26}Mn_{20}Fe_{20}Co_{20}Ni_{14}$ HEA under low-temperature and high-strain rate environments. As the temperature lowers and the strain rate rises, the alloy's YS and UTS experience substantial increases, whereas its ductility diminishes. At RT with a strain rate of 10^3 s^{-1}, the $Cr_{26}Mn_{20}Fe_{20}Co_{20}Ni_{14}$ HEA showed a yield strength (YS) of 212 MPa, an ultimate TS of 565 MPa, and an elongation of 0.73. Under LNT and a strain rate of 10^1 s^{-1}, the YS and UTS surged by 210% and 137%, reaching 656 MPa and 1337 MPa. Concurrently, the elongation decreased by 30%, down to 0.51. In LNT and high strain rate scenarios, the alloy's deformation mechanisms altered, with the development of slip bands (SF), twinning, and HCP phase transformations playing pivotal roles in the deformation process. In particular, at LNT, forming a nanotwin HCP phase composite structure helped optimize stress and strain distribution, reducing damage nucleation. However, these deformation mechanisms enhanced the strength and led to embrittlement, making interfaces (such as grain and phase boundaries more susceptible to cracking.

Semerenko et al. [142] investigated how martensitic phase transformation (DIMT) affects the properties of the $Co_{17.5}Cr1_{2.5}Fe_{55}Ni_{10}M_{o5}$ alloy during deformation at low temperatures. At RT, this alloy displays an FCC phase structure. Following annealing, the alloy undergoes complete recrystallization with randomly oriented grains, preserving the FCC crystal structure. At RT, this alloy displays an FCC. Following annealing, the alloy undergoes complete recrystallization with randomly oriented grains, preserving the FCC crystal structure. With an increasing proportion of the BCC phase, the alloy's dynamic Young's modulus rises linearly, suggesting that phase transformation boosts the mechanical properties of the alloy. At 4.2 K, the deformed alloy shows excellent mechanical performance with a YS of 1043 MPa and a TS of 1748 MPa while maintaining high plasticity. The shift from FCC to BCC and HCP phases is regarded as the primary mechanism enhancing the low-temperature strength and plasticity of the $Co_{17.5}Cr_{12.5}Fe_{55}Ni_{10}Mo_5$ alloy.

DIMT has been demonstrated to be pivotal in improving the mechanical properties of HEAs under low-temperature conditions. Moon et al. [143] performed tensile tests on the $Co_{17.5}Cr_{12.5}Fe_{55}Ni_{10}Mo_5$ alloy at temperatures of 77 K, 4.2 K, 2.1 K, and 0.5 K. They discovered that DIMT is the fundamental mechanism behind the alloy's high strength and excellent ductility. In low-temperature deformation, the FCC phase converts into HCP and BCC phases. Upon reaching a true strain of 10%, the FCC phase initiates transformation into HCP and BCC phases. As deformation progresses, the BCC proportionally increases substantially, whereas the HCP remains below 10%. The Mo5 alloy showcases a high YS of 1075 MPa and a TS of 1651 MPa. It undergoes ductile fracture, characterized by typical dimpled fracture surfaces at both 77 K and 0.5 K, signifying excellent elasticity. As the temperature decreases, the alloy exhibits DPF, and adiabatic heating during deformation promotes dislocation cross-slip and DIMT. Nevertheless, as the temperature continues to drop, these deformation mechanisms are progressively inhibited. At temperatures below 4.2 K, the alloy's YS becomes highly temperature dependent. Dislocation motion seems to be affected by inertial mechanisms, resulting in atypical dislocation behavior and further complicating deformation processes. DIMT is vital for the ductility of the Mo5 alloy, as it effectively mitigates strain localization, thereby sustaining excellent flexibility even at extremely low temperatures.

Scientists have undertaken studies to tailor the low-temperature properties of HEAs through the incorporation of non-metallic modifying elements. Yang et al. [137] investigated deformation mechanisms of Fe-based HEAs incorporating carbon and silicon across various temperatures. By incorporating 1% carbon and silicon into the $Fe_{53}Mn_{29}Co_9Cr_9$ HEA, they modified the stacking fault energy (SFE) to 33.96 mJ/m^2, achieving a single-phase FCC structure. The De-HEAs showcased high strength and excellent ductility at RT. When tested at 223 K, the alloy's YS rose to 907 MPa, and its elongation enhanced to 69.6%. The improvement in the alloy's performance was mainly due to alterations in its deformation mechanisms under low-temperature conditions. Lowering the temperature led to a notable rise in the alloy's strain hardening rate, causing the deformation mechanism to shift from dislocation slip to twinning. As the strain increased, secondary nanotwins began to form and activate. Secondary nanoscale twins developed within the alloy's dislocation framework, promoting grain refinement and enhancing the material's strength and plasticity. Refer to Figure 7 for details, TEM analysis indicated that secondary nanotwins formed within dislocation clusters during low-temperature deformation, increasing the strain-hardening capacity and contributing to improved hardness and flexibility. At low temperatures, the De-HEAs demonstrated a higher strain-hardening ability than conventional metals, especially through the formation of twins and the interactions between dislocations. KAM map analysis revealed that the increase in secondary nanotwins and

dislocation density significantly enhanced the strain hardening, improving the alloy's mechanical performance.

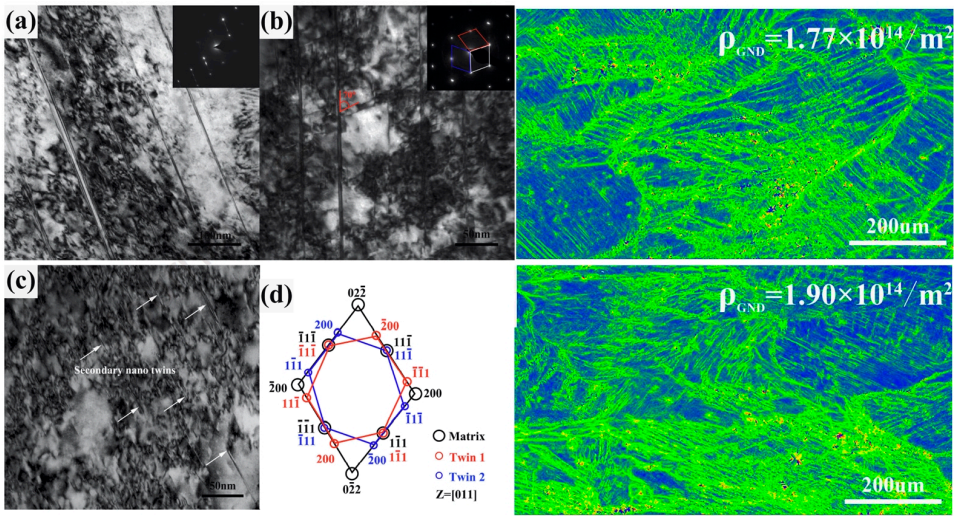

Figure 7. Tensile deformation structures of the alloy at 223 K. (**a**) Primary deformation twin formation; (**b**,**c**) secondary nanoscale twin development; (**d**) indexed results illustrating twin orientations and strain conditions [137].

Regarding manufacturing techniques, researchers [144] have utilized laser melting deposition (LMD) technology to prepare non-equimolar CoCrFeNiMo$_{0.2}$ HEA and investigate their low-temperature mechanical properties. The findings indicated that varying laser power notably influenced the microstructural characteristics of the alloy. As the laser power increased, the columnar grains grew and exhibited noticeable anisotropy. At 1400 W, the orientation and growth of the columnar grains became more pronounced. At 293 K, enhancing the laser power led to a considerable increase in plasticity, from 37% to 51%, along with an improvement in TS. When tested at 77 K, the alloy exhibited a substantial increase in TS to 928 MPa, and flexibility reached 60% under a laser power of 1400 W. Examination of the fracture surfaces revealed characteristic ductile fracture patterns at both 293 K and 77 K. At 77 K, the fracture surfaces exhibited larger dimples and deeper tear marks, indicating an enhanced ability to deform plastically at low temperatures. Fracture surface examination revealed (Figure 8) typical ductile fracture features at both 293 K and 77 K. At 77 K, the fracture surfaces displayed larger and deeper dimples and tear marks, indicating enhanced plastic deformation at low temperatures. Additionally, the side surface at 77 K showed more slip traces compared to 293 K, suggesting the activation of additional slip systems and increased plasticity. The study highlights the influence of laser power on the microstructure and performance of the alloy, demonstrating the potential of CoCrFeNiMo$_{0.2}$ high-entropy alloy as a coating material for low-temperature applications.

3.2. BCC-Phase HEAs

Crystal dislocation movement is more challenging in the BCC than in the FCC. BCC crystals have only a few slip systems, making them less likely to undergo large-scale plastic deformation at RT. However, under low-temperature conditions, with appropriate composition design, BCC single-phase HEAs can enhance their plasticity and toughness through mechanisms such as twinning or phase transformation, thereby improving their resistance to brittle fracture. The earliest study [125] of BCC-phase HEAs at cryogenic temperatures was conducted by Huang et al. in 2011 on AlCoCrFeNi HEA. The study examined the compressive and tensile behaviors of the BCC-phase alloy at both room and cryogenic temperatures. It was observed that lowering the temperature from 298 K to 77 K

resulted in a 29.7% increase in YS and a 19.9% rise in fracture strength. Additionally, the fracture mode transitioned from intergranular at 298 K to transgranular at 77 K.

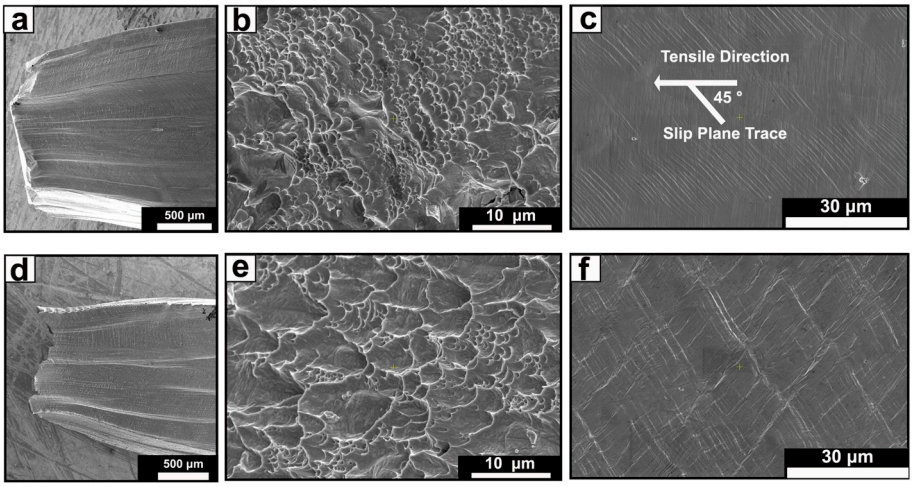

Figure 8. Fracture surface appearances under various conditions. (**a**) Entire fracture view at 293 K; (**b**) detailed fracture morphology at 293 K; (**c**) side view of the sample at 293 K; (**d**) entire fracture view at 77 K; (**e**) detailed fracture morphology at 77 K; (**f**) side view of the sample at 77 K [144].

Leveraging the mechanical characteristics of HEAs in cold environments, researchers have explored how low-temperature conditions influence the machining quality and mechanical properties of $FeCoCrNiAl_{0.6}$ HEA. The research indicates that higher cutting speeds enhance the surface quality of specimens at RT, whereas greater cutting depths lead to a deterioration in surface finish. In low-temperature conditions at 153 K, increasing cutting speed also improves surface quality, which is superior to machining at RT. Increasing the speed from 2000 to 2800 mm/min notably diminishes chip adhesion and pile-up edges. Additionally, the area covered by surface pits and defects is reduced, resulting in significantly better surface quality. Figure 9 displays the alloy's surface morphology post-machining under various temperature conditions. Figure 9a,b illustrate the alloy's surface after machining at RT, showing prominent built-up edges and pit defects that compromise surface integrity. Conversely, Figure 7c,d present the surface morphology following machining at low temperatures. Here, the surface quality is notably enhanced, with fewer built-up edges and pit defects, leading to a smoother finish.

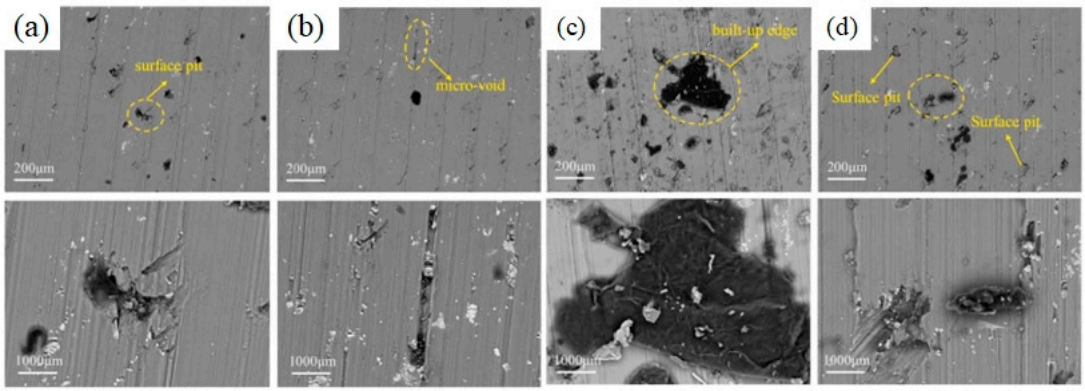

Figure 9. Surface morphology of the alloy post-machining. (**a**) Cutting speed (vc) = 2000 mm/min at RT; (**b**) vc = 2200 mm/min at RT; (**c**) vc = 2000 mm/min at low temperature; (**d**) vc = 2200 mm/min at low temperature [125].

In terms of fatigue performance, increasing cutting speed enhances fatigue life. At a cutting speed of 2000 mm/min, the fatigue life at RT is 142,100 cycles, while at 153 K, it increases to 319,071 cycles. Although increasing cutting depth reduces fatigue life, fatigue life under low-temperature cutting conditions remains significantly better than at RT. Concerning mechanical properties, when the cutting speed is set to 2000 mm/min, both YS and TS at low temperatures are enhanced by 6.2% and 10.4%, respectively, relative to those measured at RT. Therefore, machining $FeCoCrNiAl_{0.6}$ HEA in low-temperature environments is feasible and can improve machining quality, mechanical properties, and fatigue life.

The refractory HEA iZrHfNbTa comprises a single BCC phase. According to Wang et al.'s [145], at 77 K, the alloy preserves a tensile elongation of 20.8%, demonstrating increase in YS, reaching 1549 MPa, without any noticeable ductile–brittle transition. At RT, the alloy's deformation mainly occurs through dislocation slip. In contrast, at low temperatures, the deformation mechanisms include the formation of nanoscale twins, phase transformation induced by deformation, and dislocation slip. Under applied stress, ω-phase precipitates emerge along the twin boundaries. Mechanical twinning and ω-phase transformation begin within a temperature window of approximately 227–277 K. HU et al. [146] observed that when tested at 77 K, the alloy retained a ductile fracture pattern despite being subjected to high strain rates. Compression testing revealed that elevating the strain rate from 400 s^{-1} to 2600 s^{-1} raised the flow stress from 1294 MPa to 1760 MPa, demonstrating a clear strain-rate strengthening effect. At 77 K and a strain rate of 2600 s^{-1}, the TiZrHfNbTa HEA exhibited a mixed-mode fracture surface, combining features of both ductile and brittle behavior.

3.3. Multi-Structural HEAs

By controlling the composition of HEAs, multi-structural alloys with excellent properties can be produced. These alloys consist of a softer matrix, typically FCC, with harder phases like σ, L12, BCC, and sometimes HCP structures. Small grain size and precipitated hard phases at low temperatures help suppress twinning, making the material more stable. The strength and toughness of these alloys arise from several mechanisms, including stacking fault strengthening, phase transformation toughening, second-phase strengthening, and precipitation strengthening. Together, these mechanisms provide high strength and toughness at low temperatures, enhancing resistance to brittle fracture. Hee et al. [147] designed an iron-rich $VC_xMnFeCoNi$ HEA. As the manganese content rose, structural stability diminished, leading to the emergence of a brittle intermetallic σ phase. At ambient conditions, this HEA has a YS of 544 MPa, which climbs to 766 MPa at 77 K. The elongation at RT is 46.2%, improving to 54.1% at low temperatures. However, as the manganese content increases, the improvement in elongation at low temperatures becomes smaller. Introducing the σ phase enhances alloy strength by anchoring grain boundaries and impeding their movement. Still, it also suppresses the formation of twinning, which reduces the flexibility at low temperatures. The σ phase's pinning effect on the grain boundaries helps to inhibit grain sliding and dislocation motion, thereby enhancing the material's strength.

Such phase transformation mechanisms and the influence of grain boundary pinning are crucial factors to designing HEAs with enhanced low-temperature properties, as demonstrated in the study by Hee et al. [147]. They designed an iron-rich $VC_xMnFeCoNi$ HEA. As Mn concentration rose, the alloy's crystalline framework grew less stable, eventually producing a brittle σ intermetallic phase. Under room-temperature conditions, the alloy's YS measures 544 MPa, rising to 766 MPa when cooled to 77 K. The elongation at RT is 46.2%, improving to 54.1% at low temperatures. However, as the manganese content increases, the improvement in elongation at low temperatures becomes smaller. By forming the σ

phase, the alloy gains strength as these precipitates effectively anchor grain boundaries and hinder their motion. Still, it also suppresses the formation of twinning, which reduces the flexibility at low temperatures. The σ phase's pinning effect on the grain boundaries helps to inhibit grain sliding and dislocation motion, thereby enhancing the material's strength.

Non-equimolar composition design has also been studied to improve low-temperature properties in high-entropy alloys. Zhang et al. [148] engineered a $Fe_{28.2}Ni_7Co_{11}Al_{2.5}Ta_{0.04}B$ HEA and employed thermomechanical treatments to achieve a heterogeneous microstructure comprising an FCC matrix and a γ′ phase, where NiAl B2-type particles precipitated along grain boundaries. Under ambient conditions, the alloy's TS reaches 1.43 GPa, accompanied by 21% elongation. Cooling to 77 K elevates the TS to around 2.2 GPa, while leaving the alloy's ductility largely unaffected. The strain hardening rates at 77 K and 298 K are over 15 GPa and 4 GPa, respectively.

Figure 10 illustrates the martensitic transformation process in the $Fe_{28.2}Ni_7Co_{11}Al_{2.5}Ta_{0.04}B$ HEA under different tensile strains. At approximately 7% tensile strain (Figure 10a), residual martensitic regions are mainly observed in the fine-grain areas, as indicated by the blue arrows. These findings imply that localized stress concentrations in fine-grained regions propel the transformation, highlighting the heterogeneous structure's uneven deformation behavior. As the strain increases to about 12% (Figure 10b), martensite almost completely extends throughout the fine-grain regions. Also, it spreads into the coarse-grain regions, as indicated by the red arrows. By adopting a staged martensitic transformation sequence, the alloy averts a premature grain-boundary failure, ultimately improving its overall ductility. The images in Figure 10c,e show two different martensitic variants, with the thickness of the martensite in the coarse-grain region being approximately 50 nm and in the fine-grain region approximately 200 nm. Figure 10d,f show a dense network of nanotwins forming in the martensitic regions, featuring twin spacings of roughly 6–10 nm and minimal stacking fault presence at twin interfaces. The twin boundaries serve as potent barriers to dislocation motion, thereby reinforcing the alloy's strain-hardening capacity under cryogenic conditions. Moreover, at 77 K the alloy demonstrates pseudoelasticity: following martensitic transformation under load, it reverts to its original austenitic state once unloaded, exhibiting superelastic-like recovery characteristics.

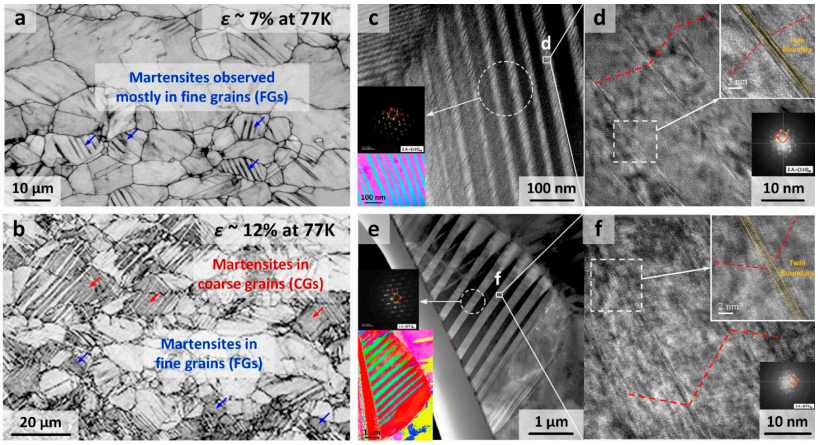

Figure 10. The microstructure of $Fe_{28.2}Ni_7Co_{11}Al_{2.5}Ta_{0.04}B$ HEA after tensile testing at 77 K. (**a**) Martensite forms mainly in fine grains at ~7% strain. (**b**) At ~12% strain, martensite spreads to fine and coarse grains. (**c**) TEM shows thin-plate martensite in coarse grains. (**d**) High-resolution TEM shows nanotwins in martensite. (**e**) TEM shows thin-plate martensite in fine grains. (**f**) Nanotwins in fine-grain martensite [147].

Drawing upon insights into low-temperature phase transformations, Bhattacharjee et al. [127] conducted a comprehensive analysis of the microstructure and mechanical behavior of the $AlCoCrFeNi_{2.1}$ EHEA under various deformation temperatures. The EHEA

develops a finely layered microstructure featuring alternating L12 and B2 phases with mean thicknesses of about 600 nm and 200 nm. Cooling triggers a phase shift in the L12 regions, causing them to revert into a disordered FCC configuration. At temperatures around 363 K and 423 K, the B2 phase retains its ordered BCC structure. However, at lower temperatures, particularly at 77 K, the L12 phase completely disorder and transforms into a disordered FCC phase. TEM analyses (Figure 11) confirm that the B2/FCC phase boundary remains notably smooth and uninterrupted, the yellow arrows indicate the lattice bands.

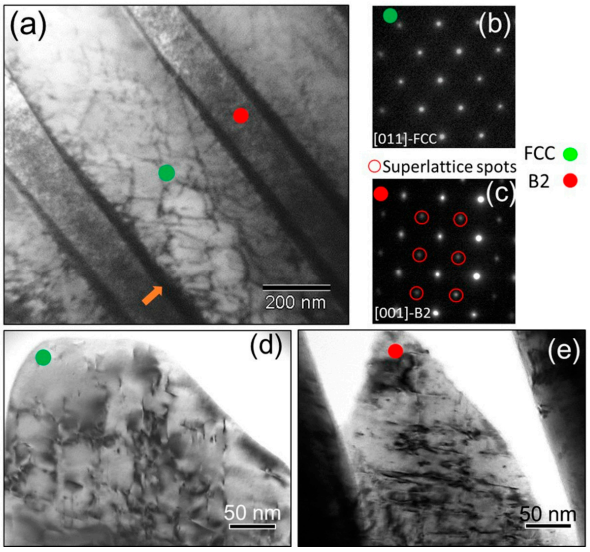

Figure 11. (**a**) The AlCoCrFeNi2.1 alloy fractured in tension at 77 K, (**b**) a SAED pattern from the area indicated by a green marker, and (**c**) an SAED pattern from the region indicated by a red marker. At higher magnifications, dislocation arrangements are clearly visible in both the (**d**) FCC and (**e**) B2 domains [127].

As deformation temperature drops, yield and ultimate TSs both rise. Meanwhile, total elongation, holding steady at around 17%–20%, shows little sensitivity to the colder environment. At low temperatures, the dislocation movement in the alloy is suppressed, making plastic deformation more difficult, enhancing strain hardening and increasing strength. Additionally, transforming the L12 phase to the disordered FCC phase at low temperatures makes the FCC phase more ductile and tougher, contributing to improved strength and retained ductility.

Although the B2 phase is typically harder to deform, it also experiences strain hardening at low temperatures, likely due to the interaction between the B2 and FCC phases at their interfaces. A profusion of dislocations accumulates along the B2/FCC interface, suggesting that their mutual interaction aids the B2 phase in accommodating plastic deformation under cryogenic conditions. Cooperative strain-hardening contributions from both the disordered FCC and B2 phases confer exceptional low-temperature mechanical properties to the $AlCoCrFeNi_{2.1}$ EHEA.

4. High-Temperature Properties of HEAs

High-temperature investigations into HEAs initially targeted the stringent requirements for robust strength and superior structural stability, particularly crucial in aerospace applications [149]. Researchers aimed to develop high-temperature materials superior to traditional high-nickel superalloys. Starting in 2010, refractory HEAs [150] became a key focus of study. Subsequently, researchers [135] employed advanced manufacturing techniques, such as powder metallurgy and laser melting deposition, to develop HEAs suitable for high-temperature environments. The scope of research has expanded, includ-

ing applications in coatings and low-density alloys, to meet various industries' specific requirements. In high-temperature environments, the performance of HEAs includes not only strength and structural stability but also key properties such as thermal stability, friction performance, and oxidation resistance. Refining these attributes is pivotal for ensuring dependable performance in aerospace, energy systems, and other high-temperature technologies. This section surveys key investigations into both transition metal-based and refractory HEAs at elevated temperatures, organizing the findings according to their elemental placements in the periodic table.

4.1. Transition Metal HEAs

In studying the high-temperature performance of transition metal HEAs, single-phase HEAs mainly focus on the FCC-phase CoCrFeMnNi alloy. However, due to the relatively low strength of the FCC phase, research has primarily concentrated on enhancing the alloy's high-temperature performance through methods such as precipitate strengthening and phase transformation strengthening. This section will present the related research findings, focusing on single-phase and multi-phase HEAs.

4.1.1. Single-Phase HEA

As previously noted, Kim et al. [135] examined the tensile behavior of CoCrFeMnNi HEAs over an extensive range of temperatures. Later efforts concentrated on uncovering how the alloy's intrinsic deformation mechanisms evolve under high-temperature conditions. Ghosh et al. [151] delved into the dynamic recrystallization (DRX) processes in CoCrFeMnNi HEAs, examining temperatures from 950 °C to 1100 °C under strain rates of 10^{-2} s^{-1} and 10^{-1} s^{-1}. Figure 12 presents the true stress–true strain profiles across various temperatures (K) and strain rates. Under a 10^{-2} s^{-1} strain rate, increasing the temperature progressively lowers the flow stress. The stress–strain response shows distinct peak stresses at strains of about 0.18, 0.20, and 0.23.

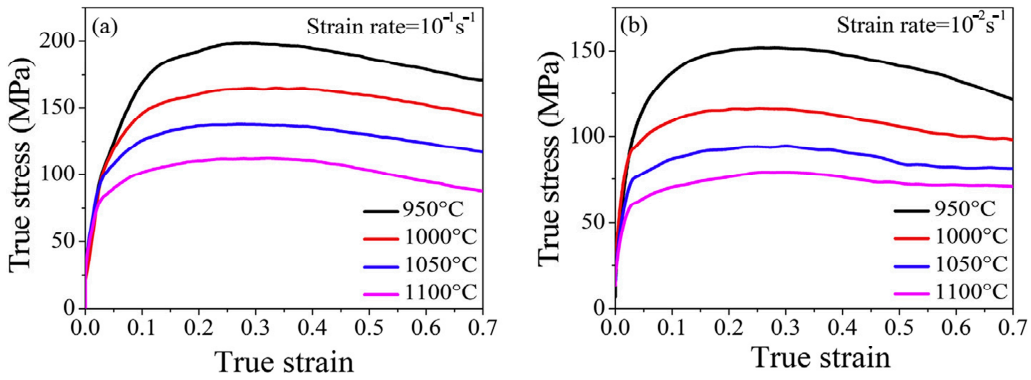

Figure 12. Stress–strain relationships for the HEA under varying thermal conditions at strain rates of (**a**) 10^{-1} s^{-1} and (**b**) 10^{-2} s^{-1} [135].

After reaching the peak value, the flow stress begins to soften and eventually reaches a steady state, with steady-state strains of 0.45, 0.5, and 0.6. This indicates that the DRX process is more complete at lower strain rates, leading to stress softening and dynamic equilibrium. Similarly, at 10^{-1} s^{-1}, the flow stress curve peaks before declining continuously without stabilizing, dropping off until the strain approaches roughly 0.7. This suggests that the DRX process is not fully developed at higher strain rates, and the dislocation density has not been effectively reduced. Overall trends indicate that heightened strain rates raise flow stress, while elevated temperatures diminish it. Lower strain rates and higher K promote the occurrence of dynamic recrystallization, leading to stress softening and the emergence of steady-state behavior. It can be observed that at high K, dynamic recrystallization causes

changes in grain size and induces significant changes in the microtexture. A higher DRX volume fraction and more pronounced microstructural evolution are observed under low strain rate conditions.

Jiang et al. [152] also probed the high-temperature oxidation characteristics of the CrMnFeCoNi HEA. Post-oxidation examinations uncovered numerous pores dispersed within the oxide scale. While these pores correlate strongly with oxide crystallization, they cannot be attributed to the Kirkendall effect. Moreover, mismatches in thermal expansion coefficients between the substrate and oxide layers induce residual stresses, ultimately causing cracks and partial delamination of the oxide scale. The alloy undergoes three main oxidation stages at high temperatures. At even higher temperatures (1050–1150 °C), thermal stresses and expansion disparities lead to spallation, progressively thinning the oxide layer. In the medium-temperature stage (950–1050 °C), the oxide layer gradually thickens due to the chemisorption of oxygen atoms. Finally, in the high-temperature stage (1050–1150 °C), the oxide layer peels off due to thermal stress and differences in the coefficient of thermal expansion, resulting in a thinning of the oxide layer. Cross-sectional analysis revealed a layered oxide structure: an outermost zone enriched in $MnFe_2O_4$ and Mn_3O_4, an intermediate $(Mn, Cr)_xO_4$ region, and an inner Cr_2O_3 layer. While FCC-phase HEAs show some resistance to high-temperature oxidation, there is still significant potential for improvement. It is evident that the high-temperature performance of single-phase FCC HEAs still requires further improvement to meet the demands of applications in extreme environments.

4.1.2. Multi-Phase HEA

In contrast to single-phase alloys, multi-phase HEAs gain reinforcement through minor additions (e.g., Al, Ti, Ta, Nb) that precipitate strengthening second phases. This approach allows the alloy to achieve higher strength and exhibit excellent thermal stability and oxidation resistance within specific temperature ranges. For instance, incorporating Al and Ti fosters the formation of γ' precipitates (e.g., Ni_3Al), bolstering both the alloy's high-temperature resilience and thermal stability. Moreover, certain alloy systems further improve performance by forming eutectic structures. By adjusting the composition, EHEAs can introduce fine reinforcing phases into the matrix, effectively hindering dislocation motion and improving the alloy's YS, creep resistance, and high-temperature durability.

As previously discussed, single-phase HEAs like CoCrFeMnNi have shown potential in high-temperature applications. However, they often require further enhancement due to their relatively low strength in high-temperature environments. In this context, Joseph et al. [153] investigated the design of Co-Cr-Fe-Ni-Al-Ti HEAs (HEAs), particularly focusing on alloys with up to 20% Al and Ti content. At 1073 K, these alloys achieve a stable $\gamma + \gamma'$ phase equilibrium structure, resulting in a high-entropy γ phase matrix. While raising the (Al + Ti) concentration elevates γ' phase volume and strength, it must remain under 18% to maintain uniform particle dispersion and prevent performance degradation. Keeping the Al/Ti ratio within 0.8–3 effectively inhibits the formation of brittle intermetallics (e.g., NiAl, Ni_2AlTi, Ni_3Ti), thereby preserving the alloy's favorable mechanical properties.

Moreover, restricting Fe, Cr, and Co within certain compositional boundaries helps avert the emergence of detrimental phases such as σ. This alloy exhibits strength retention of over 873 MPa at 1073 K, with an anti-coarsening performance comparable to some commercial high-temperature alloys. Furthermore, it does not contain expensive elements such as Re or Ta, which offers a cost-effectiveness advantage.

Based on this, Joseph et al. [154] developed $Ni_{51}Co_{18}Fe_5Cr_{10}Al_{16}$-XTiX HEAs. Exceeding 60% in γ'-phase volume, this alloy maintains a robust γ/γ' equilibrium field between 1073 K and 1173 K. Notably, no residual brittle intermetallics (e.g., Ni_2AlTi, Ni(Al, Ti), Ni_3Ti,

σ) are detected, confirming its strong thermal stability at elevated temperatures. By selecting an Al-to-Ti ratio between 0.8 and 3, the alloy achieves a substantial γ′-phase fraction, a γ′ solvus above 1457 K, and a broad equilibrium range for the γ/γ′ phases. Mechanically, this composition surpasses 800 MPa in TS across the 1073–1173 K interval. Although raising Ti levels can initially lower the solidus temperature, adjusting the Ti content or the Al/Ti ratio can boost both the γ′ fraction and the solidus temperature, granting more flexibility in tuning the alloy's high-temperature behavior. The study also revealed that reducing the aluminum-to-titanium ratio improves the YS. In $Ni_{51}Co_{18}Fe_5Cr_{10}Al_8Ti_8$, pronounced lattice mismatch between γ and γ′ phases, together with fine precipitates, augments precipitation hardening and elevates its YS. In summary, fine tuning the Al/Ti ratio refines the alloy's microstructure and enhances performance by boosting γ′-phase content, widening the γ′ stability domain, and raising YS.

Similarly, Zhang et al. [155] examined γ-reinforced $Ni_{45}x(FeCoCr)_{40}(AlTi)_{15}Hf_x$ (x = 0, 0.2) HEAs, featuring a high-entropy γ matrix and uniformly dispersed γ′ precipitates in their as-cast state. Their γ′ precipitates average about 52 nm within dendritic arms and roughly 90 nm in interdendritic areas. Enriched with γ′ precipitates, these alloys maintain superior mechanical attributes at both ambient and elevated temperatures. For example, $Ni_{44.8}(FeCoCr)_{40}(AlTi)_{15}Hf_{0.2}$ delivers an impressive 961.6 MPa at 750 °C and retains 696.6 MPa at 1123 K. Remarkably, the $Hf_{0.2}$ variant achieves strength levels rivaling traditional Ni-based superalloys—without Mo, W, or carbide additions. The γ′ phase fortifies the alloy at high temperatures through coherency-driven reinforcement and the stability of its ordered lattice.

Jaladurgam et al. [128] examined as-cast $AlCoCrFeNi_{2.1}$ EHEA at 973 K, investigating how load sharing shifts between $L1_2$ and B2 phases under high-temperature deformation. Their findings reveal a temperature-dependent role reversal: at low temperatures (77–673 K), $L1_2$ is weaker, but at 973 K it emerges as the primary strengthening phase. In contrast, the B2 phase exhibited low strength and nearly ideal plastic behavior, indicating a significant change in its deformation mechanism at elevated temperatures. Figure 13 depicts the alloy's lamellar architecture in the as-cast state alongside its 973 K stress–strain response, featuring a 216 MPa YS.

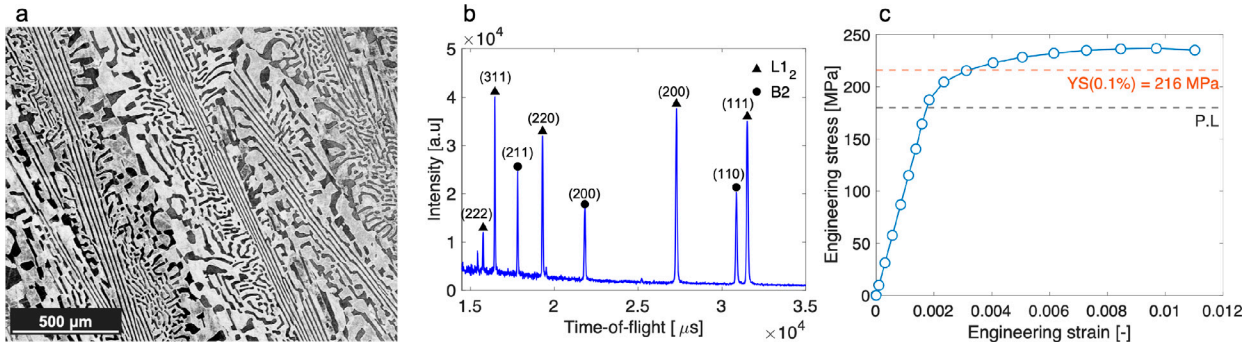

Figure 13. (**a**) The $AlCoCrFeNi_{2.1}$ microstructure, (**b**) compositional mappings, and (**c**) its stress–strain curve at 973 K [135].

They also established that cube slip predominates in $L1_2$, causing [111]-oriented grains—aligned perpendicularly to the tensile direction—to yield prematurely in early deformation. As deformation progressed, these grains gradually lost their load-carrying capacity, with the load being progressively transferred to grains with [200] and [311] orientations. In contrast, the stress distribution across orientations in the B2 phase showed no significant load transfer, differing markedly from its behavior at low temperatures.

Additionally, the experiments detected possible twinning in the alloy, but its influence appeared to be limited, with cube slip remaining the primary deformation mechanism.

In the field of coatings, Joseph et al. [156] studied the wear resistance and mechanisms of $Al_xCoCrFeNi$ coatings (x = 0.3, 0.6, 1.0 at %) across a temperature range from room temperature to 900 °C. The steady-state friction coefficient decreased with increasing temperature for all HEA coatings. Among them, AlCoCrFeNi demonstrated the highest wear resistance at all tested temperatures. At 600 °C and 800 °C, its wear performance matched that of Inconel 718, and at 900 °C, the $Al_xCoCrFeNi$ coatings (x = 0.3, 0.6, 1.0) outperformed Inconel 718. At 900 °C, it was observed that coatings with lower aluminum content developed an outer Cr_2O_3 oxide layer and an inner Al_2O_3 layer, whereas higher aluminum content resulted in a dense Al_2O_3 oxide layer. Sub-surface analysis beneath the oxide layer revealed the presence of Cr-rich precipitates in AlCoCrFeNi coatings between 600 °C and 900 °C, with precipitate size increasing at higher temperatures. Furthermore, prolonged exposure to temperatures between 600 °C and 960 °C led to the formation of a body-centered tetragonal σ phase, which enhanced the mechanical properties of CoCrFeNi.

Ma et al. [157] studied $W_{0.5}Ta_{0.3}MoNbVAlTi_{1-x}Zrx$ (x = 0, 0.25, 0.5, 0.75, 1.0) HEA coatings and found that increasing x had little effect on hardness but greatly improved oxidation resistance. After 20 h at 800 °C, the coating with x = 0.75 showed the best performance, about 6.2 times better than x = 0. The coatings developed a two-layer oxide structure. The outer layer mainly contained Fe_2O_3, FeO, and V_2O_5, while the inner layer composition varied with x. Higher x reduced V in the outer layer and decreased TiO_2 and MoO_3 in the inner layer. The high PBR values of V_2O_5 and MoO_3 indicated zirconium minimized unstable oxides. Additionally, the dense Al_2O_3 film in the inner layer prevented metal diffusion, enhancing stability.

4.2. Refractory HEAs

Conventional high-temperature alloys typically consist of an unordered FCC matrix, which can incorporate nanoscale precipitates or an ordered FCC (L12) structure, enabling good performance at elevated temperatures. In contrast, refractory HEAs feature an unordered BCC matrix and form similar microstructures, further enhancing their high-temperature properties. Additionally, these alloys can be strengthened using traditional high-temperature methods, such as heat treatment, which precipitates hard secondary phases that effectively hinder dislocation movement, thereby increasing strength. These structures and processing techniques allow refractory HEAs to withstand greater forces and pressures at high temperatures while maintaining superior mechanical properties. As a result, refractory HEAs have risen to prominence as advanced high-temperature structural materials, prompting extensive research into their mechanical robustness, thermal stability, and oxidation resilience.

4.2.1. Mechanical Properties

In line with the findings on refractory HEAs, studies have explored these alloys' mechanical performance and deformation behavior at high temperatures. For example, Wang et al. [158] showed that VxNbMoTa, a single-phase BCC refractory HEA, maintains structural consistency from its melting point down to 623 K. Higher V concentrations lead to markedly finer grain dimensions. For instance, boosting V content from 0.25 to 1.0 shrinks the grain size from roughly 830 μm to about 250 μm. At 1273 K, VNbMoTa attains a YS of 811 MPa, while at room temperature it can sustain more than 25% tensile fracture strain, exemplifying remarkable strength–ductility synergy.

In parallel work, Couzinié et al. [159] probed deformation mechanisms in $Al_{0.5}Nb Ta_{0.8}Ti_{1.5}V_{0.2}Zr$ at 873 K. They reported a 1186 MPa YS at 873 K and observed the nucle-

ation and growth of B2 precipitates during mechanical loading. Meanwhile, dislocations interacted with the precipitated B2 phase during deformation, particularly when a pair of a/2<111> type dislocations sheared the B2 precipitates during their motion. This shearing interaction strengthened the alloy at high temperatures, enhancing its mechanical properties and strength.

Liu et al. [160] synthesized $NbTaHfTiZrV_{0.5}$ and evaluated its mechanical attributes between ambient conditions and 1273 K. The alloy maintained a BCC structure at different deformation temperatures, with lattice constants slightly increasing with temperature. The alloy exhibited a typical dendritic structure, and its microstructure remained essentially unchanged after cold rolling and high-temperature tensile tests, with identical microhardness both inside and between dendrites. The alloy was able to maintain high YS between 873 K and 1073 K, with YSs of approximately 1141.55 MPa at 873 K, 1168.89 MPa at 973 K, and 1189.75 MPa at 1073.

Figure 14a presents tensile stress-strain profiles over various test temperatures, each initially rising to a peak before steadily tapering off as deformation proceeds. Figure 14b plots how YS, ultimate tensile strength (UTS), and fracture elongation (FE) evolve with increasing temperature. TAs temperature climbs, YS wanes from over 1200 MPa to under 1000 MPa. Interestingly, between 873 K and 1073 K, a plateau persists above 800 MPa, indicating a stable strength regime. This behavior correlates closely with changes in dislocation activity. At elevated temperatures, deformation mainly hinges on dislocation slip, making dislocation morphology and density key factors in determining mechanical performance. For instance, at 673 K the exceptionally dense, intricate dislocation networks underpin the alloy's high ductility. For instance, at 673 K the exceptionally dense, intricate dislocation networks underpin the alloy's high ductility.

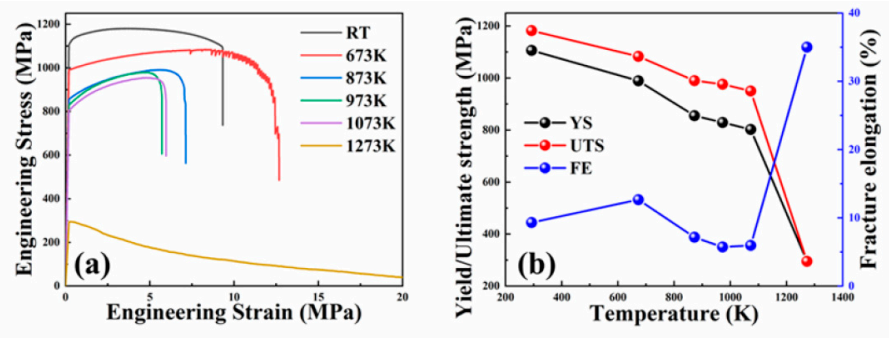

Figure 14. (**a**) Tensile stress–strain curves at various temperatures. (**b**) YS, UTS, and fracture elongation versus temperature [160].

Further exploring the wear resistance of refractory HEAs, Alvi et al. [161] utilized spark plasma sintering to fabricate the CuMoTaWV HEA, whose phase structure consists of 80% BCC solid solution and 20% FCC phase. Hardness testing revealed that the vanadium-rich regions have a hardness of approximately 900 Hv, while the high-entropy phase regions exhibit a hardness of around 600 Hv. At 298 K, this material exhibited a remarkably low wear rate (~5×10^{-7} mm^3/Nm) and a friction coefficient of 0.5 against steel balls (700–880 Hv hardness). However, the COF and wear rate showed significant temperature dependence when subjected to sliding wear tests using Si_3N_4 balls with a hardness of 1550 Hv at various temperatures. At 298 K, the wear rate was 4.0×10^{-3} mm^3/Nm with a COF of 0.45. Increasing the temperature to 473 K resulted in a substantial rise in wear rate to 2.3×10^{-2} mm^3/Nm and an increase in COF to 0.59, primarily due to adhesive wear and severe galling caused by material transfer.

At 673 K, the wear rate declined to ~5×10^{-3} mm^3/Nm while COF rose to 0.67, a shift linked to Cu oxidation generating a lubricious CuO trilayer in the wear path. At 873 K,

although COF dropped to 0.54, wear rate climbed to about 4.5×10^{-2} mm^3/Nm due to extensive oxidation of Cu, Ta, W, and the emergence of V_2O_5 in V-enriched zones. The wear rate of the opposing ball also changed with temperature, rising from 2.19×10^{-6} mm^3/Nm at 298 K to 4.94×10^{-6} mm^3/Nm at 473 K, then dropping to 2.46×10^{-6} mm^3/Nm at 673 K and 1.39×10^{-6} mm^3/Nm at 873 K. Microstructural analysis indicated that at RT, a tribolayer rich in Ta and W oxides formed within the wear track. The wear rate of the opposing ball also changed with temperature, rising from 2.19×10^{-6} mm^3/Nm at 298 K to 4.94×10^{-6} mm^3/Nm at 473 K, then dropping to 2.46×10^{-6} mm^3/Nm at 673 K and 1.39×10^{-6} mm^3/Nm at 873 K. By 873 K, Ta/W oxides and expanded V_2O_5 regions lowered COF, but rampant oxidation marginally raised the wear rate again. Overall, the CuMoTaWV HEA exhibited adaptive wear behavior across the temperature range of 298 K to 873 K. Its microstructure, and the formation of protective oxide layers at different temperatures significantly influenced its tribological performance, endowing it with excellent wear-resistant properties in high-temperature environments.

4.2.2. High-Temperature Thermal Stability

Metal materials can experience thermal degradation at high temperatures, such as softening, creep, and oxidation, which reduce their strength, hardness, and toughness. However, an effective alloy design can maintain refractory HEAs' stability and performance under high temperatures. Subsequent investigations emphasize how compositional control, microstructural refinement, and tailored processing enhance refractory HEAs' high-temperature stability.

For example, Jhong et al. [162] investigated a ternary alloy system composed of aluminum (Al), niobium (Nb), and vanadium (V), and constructed the phase diagram of the system. By performing a one-month post-annealing treatment on the alloy at temperatures of 1073 K or 1273 K, they determined the equilibrium state of the alloy. They mapped the distribution regions of various phases (such as BCC solid solution, $AlNb_2$, $AlNb_3$, Al_3Nb, and Al_3V) in the phase diagram. For example, $Al_{30}V_{35}Nb_{35}$ forms nanoscale $AlNb_2$ precipitates that lower its thermal conductivity. In the $Al_{25}V_{25}Nb_{25}Cr_{25}$ and $Al_{20}V_{20}Nb_{20}Cr_{20}Ti_{20}$ alloys, the Laves C14 phase also contributes to a reduction in thermal conductivity. He et al. [163] discovered that $CoCrFeNiNb_x$ HEAs retain a stable lamellar architecture at annealing temperatures under 873 K, underscoring their structural persistence. Even when heated to 1127 K, the lamellar framework retained commendable mechanical performance. Elevating the annealing temperature from 873 K to 1127 K softened the alloy, reducing its hardness from approximately 600 HV to 500 HV. Despite this softening, the material's compressive strength remained near 2.3 GPa, suggesting minimal alterations to its mechanical attributes at elevated temperatures.

These studies primarily focus on phase stability and microstructural evolution. At the same time, other research also investigates the influence of specific structural features, such as antiphase boundaries and nanoscale precipitates, on high-temperature properties. Pang et al. [164] examined how the $Nb_{40}Ti_{25}Al_{15}V_{10}Ta_5Hf_3W_2$ HEA resisted structural and mechanical degradation at elevated temperatures. Aging at 1023 K for 120 h prompted the development of nanoscale, Hf-rich segregations along grain boundaries. Throughout the entire aging interval (923–1123 K), the alloy largely preserved its single-phase BCC configuration. After aging for 120 h at 923 K, a high density of antiphase boundaries (APBs) appeared within the alloy. Following aging at 1023 K for 120 h, nanoscale segregations enriched with hafnium (Hf) formed at the grain boundaries. Moreover, aging at 1123 K for the same duration induced the appearance of minor tetragonal $(Nb, Hf)_2Al$ precipitates near grain boundaries and Hf-enriched zones. Figure 15 presents transmission electron microscopy (DF-TEM) images under different temperatures and aging times, specifically

showing the high density of APBs after aging for 120 h at 923 K (Figure 15a), the Hf-rich nanoscale segregations after aging for 120 h at 1023 K (Figure 15b), and both the Hf-rich segregations and tetragonal phase precipitates after aging for 120 h at 1123 K (Figure 15c). Although antiphase boundaries (APBs) were abundant at 923 K, the alloy's YS showed no meaningful reduction. Figure 15d–j is the compositional scanning image of Nb, Ti, Al, V, Ta, Hf, and W, respectively. Even with a high density of APBs at 923 K, the YS of the alloy did not exhibit significant changes. Across 923–1123 K, the $Nb_{40}Ti_{25}Al_{15}V_{10}Ta_5Hf_3W_2$ alloy exhibited remarkable structural and mechanical resilience. Its stability stemmed from a robust high-temperature microstructure and the sparse formation of low-volume precipitates, ensuring negligible effects on mechanical integrity.

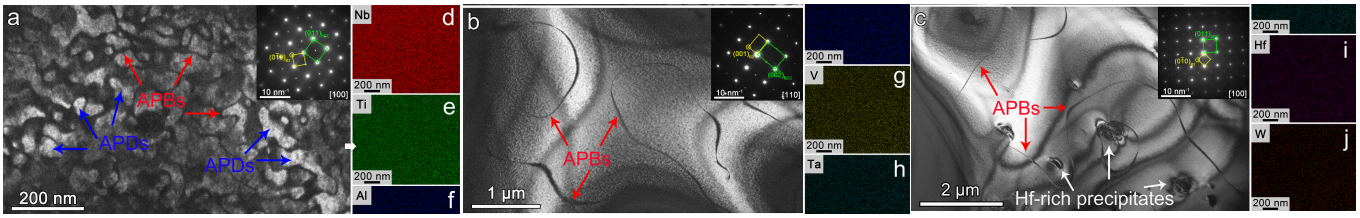

Figure 15. TEM micrographs of the $Nb_{40}Ti_{25}Al_{15}V_{10}Ta_5Hf_3W_2$ alloy after 120 h of aging at 923 K (**a**), 1023 K (**b**), and 1123 K (**c**), illustrating APB development and Hf-enriched segregations [164].

Beyond experimental efforts, computational research has probed how localized chemical ordering influences phase stability and microstructural evolution. For instance, Qiu et al. [165] employed simulations to unravel how local compositional ordering affects both structural robustness and mechanical behavior in AlNbVTiZr alloys. Their findings revealed that imposing greater atomic order boosted TS from 3.9 GPa (disordered) to 4.1 GPa (ordered), demonstrating that enhanced chemical order bolsters alloy strength. Ordering influenced thermodynamics as well: between 0 and 1500 K, the ordered arrangement showed lower configurational entropy (9.87 J/(mol·K)) than the disordered variant (13.38 J/(mol·K)), underscoring the ordered state's greater thermodynamic stability. Therefore, the ordered structure exhibits better thermodynamic stability at high temperatures than the disordered structure.

4.2.3. High-Temperature Oxidation Resistance

Refractory HEAs have improved oxidation resistance due to factors like composition, crystal structure, and surface conditions, which are influenced by alloy composition, heat treatment, and surface treatment. Elements like Cr, Al, and Ti form dense oxide layers that prevent oxygen infiltration and enhance oxidation resistance. Incorporating high-melting-point components (Hf, Mo, Nb, Ta, W, Zr) together with oxidation-resistant elements (Al, Cr, Ti, Si) notably improves the oxidation tolerance of refractory HEAs. Gorr et al. [166] investigated oxidation kinetics in W-Mo-Cr-Ti-Al, Nb-Mo-Cr-Ti-Al, and Ta-Mo-Cr-Ti-Al refractory HEAs at 1273 K and 1373 K. They found that all three alloys formed uneven, thick, porous oxide layers on their surfaces. Of these alloys, only Ta-Mo-Cr-Ti-Al showed robust oxidation resistance at both temperatures, adhering to a parabolic oxidation-rate profile. This performance arose from the formation of a thin, tightly packed alumina-enriched oxide film.

For another refractory TiZrHfNbTaV HEA [167], the focus was on its high-temperature oxidation behavior between 1073 K and 1273 K, particularly the structural characteristics of the oxide scale and its evolution at different temperatures. Oxidation tests in air were conducted at 1073 K, 1173 K, and 1273 K for one hour each. After high-temperature oxidation, the alloy maintained a BCC structure, demonstrating high stability at elevated temperatures. Under 1073 K and 1173 K conditions, the oxide surface developed a loose,

whisker-like morphology that facilitated ongoing oxygen penetration. At 1173 K, Ti and Nb were enriched in the outermost layer, promoting the formation of $TiNb_2O_7$, but the formation of HfO_2 and ZrO_2 simultaneously accompanied this. These brittle oxides tend to form microcracks and pores during the oxidation process. At 1273 K, the oxide layer was divided into an outer layer and an inner layer, with the inner layer exhibiting high porosity, which further accelerated oxygen permeation into the alloy substrate. Under these circumstances, (Hf, Zr) O_2 crystallized into a dendritic pattern that encouraged pore formation and undermined the oxide layer's protective capabilities.

Moreover, Nb and Ti segregated at the oxide surface as oxidation progressed. At the same time, Zr and Hf were depleted within the oxide layer, resulting in uneven elemental distribution within the alloy. Such elemental clustering diminished oxide density and protective efficacy, eroding the HEA's overall oxidation resistance. These findings also confirm that refractory HEAs need to optimize their alloy composition and microstructure in high-temperature oxidative environments to enhance the density and stability of the oxide layer, thereby improving their overall oxidation resistance.

5. Summary and Outlook

The present review summarizes how HEAs adapt under extreme environments and discusses how thermal treatments at both ends of the temperature spectrum refine their performance. In low-temperature environments, rational compositional design enables HEAs to achieve high flexibility and strength, with the plasticity and toughness of single-phase alloys even improving at low temperatures. Multi-phase HEAs maintain high strength, flexibility, and toughness at low temperatures. Activating deformation mechanisms such as twinning, phase transformation, and stacking faults helps to achieve superior mechanical properties with smaller strains and reduce plasticity loss. Low-temperature treatments and processing techniques can further enhance performance by controlling temperature and applying appropriate force and deformation.

HEAs exhibit superior or comparable high-temperature stability in high-temperature environments compared to traditional nickel- and cobalt-based high-temperature alloys. In transition metal multi-phase HEAs, γ' precipitate-strengthened alloys have a higher degree of alloying, significantly enhancing high-temperature strength and creep resistance. Adjustments in lattice distortion and antiphase boundary energies within the γ' phase enhance high-temperature behavior. Because of their lofty melting points and robust thermal stability, insoluble HEAs retain strong wear and oxidation resistance under hot operating conditions. The mechanical properties and durability under high-temperature conditions can be further optimized through high-temperature treatments and advanced alloy design methods.

Beyond bulk materials, coatings based on HEAs have emerged as a promising approach to enhancing performance under extreme conditions. HEA coatings demonstrate excellent thermal stability, wear resistance, and oxidation resistance at elevated temperatures, making them highly suitable for applications such as turbine blades, aerospace components, and nuclear reactors. In cryogenic environments, HEA coatings can mitigate surface embrittlement, reduce friction, and improve wear resistance, ensuring the long-term stability and durability of structural materials. Future research should focus on developing advanced fabrication methods for HEA coatings, such as additive manufacturing and thermal spraying, to enhance their performance and adaptability in extreme environments. Additionally, understanding the interfacial bonding between coatings and substrates and optimizing the microstructure of HEA coatings will be critical to improving their mechanical properties and reliability.

Although HEAs have made progress in compositional tunability and diverse deformation mechanisms, breaking through the performance limits of traditional materials, there is still room for optimization in their application under extreme conditions. Precisely controlling the microstructure and optimizing deformation mechanisms to maximize performance under extreme environments remain frontier topics in HEA research. Novel manufacturing processes such as additive manufacturing and high-pressure torsion have opened new avenues for developing HEAs while optimizing processing techniques and alloy design to better adapt to extreme environments. This is an important future research direction. Additionally, as multi-component alloys in the intermediate phase region, the compositional optimization of HEAs remains challenging. The following points need further attention:

1. The specific impact of multiple deformation mechanisms on alloy performance under extreme environments.

Numerous studies have introduced traditional material toughening mechanisms into HEAs, significantly improving their service performance. Nonetheless, pinpointing the exact roles and relative contributions of various deformation processes in harsh settings remains essential for engineering stronger, tougher HEAs. Moreover, though precipitate strengthening improves strength, prolonged aging at elevated temperatures can trigger abnormal precipitate growth and irregular dispersion, diminishing both strength and creep resistance at high temperatures. Hence, sustaining higher dislocation densities alongside effective precipitate strengthening becomes imperative. At lower temperatures, precipitate-induced reinforcement also boosts strength, yet aging can drastically lower matrix dislocation densities, ultimately depressing YS. Thus, enhancing the dislocation density in the matrix is necessary while maintaining the effect of precipitate strengthening. With the advancement of experimental and computational technologies, a deeper understanding of the interactions between residues and the matrix during deformation, dynamic recrystallization behavior, and the diffusion and partitioning mechanisms of elements at grain boundaries and phase interfaces will be achieved. This will aid in designing HEAs with excellent mechanical properties under extreme environments.

In the context of HEA coatings, various microscopic deformation mechanisms also interact with each other. Under high-temperature conditions, if precipitation strengthening occurs within the HEA coating, it is necessary to consider the effects of cyclic thermal loading or high-temperature aging on the precipitates, as well as the impact of the thermal expansion mismatch between the coating and substrate on interfacial bonding. At low temperatures, attention should be paid to the effect of precipitates on dislocation motion, the stacking fault energy, and microcrack formation within the coating. By optimizing the microstructure and precipitation distribution within the coating, the durability of the coating and the overall service performance of the substrate can be synergistically enhanced.

2. Mechanisms of toughening and plasticizing high-strength HEAs at high and low temperatures.

Although some HEAs achieve YS of up to 2 GPa, most exhibit low-temperature YSs below 1.5 GPa and do not yet outperform traditional low-temperature engineering materials. Therefore, further research on HEA's fundamental structures and deformation mechanisms is essential to enhance their low-temperature performance. Key areas include understanding the deformation mechanisms and toughening principles of ultra-high-strength FCC and BCC HEAs at low temperatures, examining the effects of different matrix structures on toughness and plasticity, analyzing phase and twin interfaces, investigating dislocation motion within the microstructure, and optimizing alloy compositions to balance toughness and strength.

At high temperatures, high-strength HEAs also face challenges with insufficient toughness and plasticity due to creep and phase transformations. Enhancing high-temperature toughness requires optimized microstructure design, such as introducing high temperature-resistant strengthening phases, designing stable gradient structures, and creating multi-phase composites. Nanoscale strengthening phases can impede dislocation movement and crack propagation, while gradient structures help disperse stress concentrations, enhancing overall toughness. Multi-phase composites synergistically improve ductility and creep resistance through interactions between different phases. Understanding these toughening mechanisms, including high-temperature dislocation dynamics and phase boundary behavior, will provide the foundation for designing HEAs with enhanced high-temperature toughness and plasticity.

HEA coatings face similar issues in terms of toughening and plasticizing. The coating may crack or delaminate under low-temperature impact loading. In high-temperature service, phase transformations or creep can reduce adhesion and durability. Therefore, strategies such as introducing nanoscale strengthening phases into the coating, optimizing interfacial bonding, and designing multilayer or gradient coating architectures can improve the coating's toughness and plasticity, thereby enhancing its overall performance under extreme temperatures.

3. Development and application of low-cost iron-based HEAs.

Due to their low cost and abundant resources, iron-based HEAs have broad application prospects. However, the compositional design of iron-based HEAs is complex, and their phase transformation behavior is more complicated to control accurately than martensitic transformations in steel. Additionally, how to reduce the number and content of alloying elements while maintaining performance remains a key issue to be addressed. Moreover, Co, Ni, and Cr, which are in the same period as iron, are high-cost elements. During development, a key research focus is how to reduce these high-cost elements while ensuring the alloy's performance under extreme environments. Iron-based HEAs can also be used to fabricate coatings, thereby reducing overall manufacturing costs and leveraging the advantages of iron-based systems, which are conducive to large-scale production.

4. Dynamic mechanical behavior and applications of HEAs at high and low temperatures.

The mechanical behavior of HEAs under dynamic loads, especially their responses under high and low-temperature environments, requires further in-depth study. Dynamic mechanical behavior involves the material's elastic and plastic responses, energy absorption, damage evolution, and fatigue performance. Integrating empirical tests with theoretical modeling can offer a comprehensive understanding of HEAs' dynamic mechanical responses across diverse temperatures and strain rates, establishing a scientific basis for their use in severe service environments. For instance, tailoring HEAs' dynamic mechanical traits for aerospace or high-velocity transport applications can improve their structural durability and operational lifespan.

The dynamic mechanical behavior of HEA coatings at high and low temperatures is even more complex. On one hand, the interface between the coating and substrate is prone to delamination or cracking under high-speed impact or abrupt temperature changes. On the other hand, the strength, ductility, and toughness of the coating itself may undergo irreversible changes under the combined effects of dynamic loading and thermal shock. Consequently, it is necessary to integrate advanced experimental methods with multiscale numerical simulations to conduct in-depth studies of the behavior of HEA coatings under high strain rates and in extreme temperature environments, thereby guiding the design, fabrication, and application of these coatings.

Author Contributions: Conceptualization, Y.L; methodology, Y.L.; validation, R.X.; formal analysis, R.X.; investigation, Y.L. and R.X.; resources, Y.L.; data curation, Y.L.; writing—original draft preparation, R.X.; writing—review and editing, R.X. All authors have read and agreed to the published version of the manuscript.

Funding: This study was supported by North China University of Water Resources and Electric Power Doctoral Research Funding (Grant Nos. 201903010). 2024 Anhui Provincial University Scientific Research Project (Natural Science Category, Key Project, No. 2024AH052003); 2024 Provincial Department of Education Science and Engineering Teachers' Internship Program in Enterprises (No. 2024jsqygz76).

Conflicts of Interest: The authors declare no conflicts of interest.

References

1. Grilli, M.L.; Valerini, D.; Slobozeanu, A.E.; Postolnyi, B.O.; Balos, S.; Rizzo, A.; Piticescu, R.R. Critical Raw Materials Saving by Protective Coatings under Extreme Conditions: A Review of Last Trends in Alloys and Coatings for Aerospace Engine Applications. *Materials* **2021**, *14*, 1656. [CrossRef] [PubMed]
2. Bondarenko, Y.A.; Kolodyazhnyy, M.Y.; Surova, V.A. Creation of High-Temperature Heat-Resistant Alloys Based on Refractory Matrices and Natural Composites. *Inorg. Mater. Appl. Res.* **2021**, *12*, 1157–1163. [CrossRef]
3. Martin, J.H.; Ashby, D.S.; Schaedler, T.A. Thin-walled high temperature alloy structures fabricated from additively manufactured polymer templates. *Mater. Des.* **2017**, *120*, 291–297. [CrossRef]
4. Krämer, A.; Lung, D.; Klocke, F. High Performance Cutting of Aircraft and Turbine Components. In Proceedings of the 4th Manufacturing Engineering Society International Conference (MESIC 2011), Cadiz, Spain, 21–23 September 2011.
5. Promakhov, V.; Matveev, A.; Schulz, N.; Dronov, P.; Zhukov, A.; Vorozhtsov, A. Structure, Properties and Phase Composition of Composite Materials Based on the System NiTi-TiB_2. *Materials* **2022**, *15*, 5327. [CrossRef]
6. Zhou, Q.; Itoh, G.; Niiromi, M. Mechanical properties and high temperature deformation of beta titanium alloys. In Proceedings of the 2006 BIMW: 2006 Beijing International Materials Week, Beijing, China, 25–30 June 2006.
7. Zhang, Q.H.; Chang, Y.J.; Gu, L.; Luo, Y.S.; Ge, B.H. Study of microstructure of nickel-based superalloys at high temperatures. *Scr. Mater.* **2017**, *126*, 55–57. [CrossRef]
8. Kablov, E.N.; Karpov, Y.A.; Titov, V.I.; Karfidova, K.E.; Kudryavtseva, G.S.; Gundobin, N.V. Rhenium and ruthenium determination in nanostructured high-temperature alloys for aerospace engineering. *Inorg. Mater.* **2015**, *51*, 1363–1369. [CrossRef]
9. Zhou, H.; Liu, X.; Jiao, H.; Ni, T.; Zhao, Y.; Wei, H. Development Strategy of Deep-Sea Exploration and Residence Equipment. *Strateg. Study CAE* **2024**, *26*, 15–22. [CrossRef]
10. Zhou, H.Y.; Jiao, P.C.; Lin, Y.T. Emerging Deep-Sea Smart Composites: Advent, Performance, and Future Trends. *Materials* **2022**, *15*, 6469. [CrossRef]
11. Santos BM, O.; Dias FJ, M.; Trillaud, F.; Sotelo, G.G.; de Andrade, R. A Review of Technology Readiness Levels for Superconducting Electric Machinery. *Energies* **2023**, *16*, 5955. [CrossRef]
12. Balint, T.S.; Cutts, J.A.; Kolawa, E.A.; Peterson, C.E. Extreme environment technologies for space and terrestrial applications. In *Space Exploration Technologies*; SPIE: Orlando, FL, USA, 2008.
13. Patterson, R.L.; Hammoud, A.; Dickman, J.E.; Gerber, S.; Elbuluk, M.; Overton, E. Electronics for deep space cryogenic applications. *J. Phys. IV* **2002**, *12*, 207–210. [CrossRef]
14. Jovičević-Klug, P.; Jovičević-Klug, M.; Podgornik, B. Unravelling the Role of Nitrogen in Surface Chemistry and Oxidation Evolution of Deep Cryogenic Treated High-Alloyed Ferrous Alloy. *Coatings* **2022**, *12*, 213. [CrossRef]
15. Wu, P.F.; Gan, K.F.; Yan, D.S.; Li, Z.M. The Temperature Dependence of Deformation Behaviors in High-Entropy Alloys: A Review. *Metals* **2021**, *11*, 2005. [CrossRef]
16. Pillai, R.; Ren, Q.; Su, Y.F.; Kurfess, R.; Feldhausen, T.; Nag, S. Leveraging Additive Manufacturing to Fabricate High Temperature Alloys with Co-Designed Mechanical Properties and Environmental Resistance. *J. Eng. Gas Turbines Power-Trans. ASME* **2024**, *146*, 061018. [CrossRef]
17. Rahman SS, U.; Wieland, H.U.; Burstein, V.; Hubner, M. High performance all metal telescope for satellite based laser communication terminals. In *Sensors and Systems for Space Applications XV*; SPIE: Orlando, FL, USA, 2022.
18. Li, Y.; Jiang, X.; Wang, X.; Leng, Y. Integration of hardness and toughness in (CuNiTiNbCr)Nx high entropy films through nitrogen-induced nanocomposite structure. *Scr. Mater.* **2024**, *238*, 115763. [CrossRef]
19. Wang, Z.Y.; Xue, S.B.; Long, W.M.; Wang, B.; Wang, J.H.; Zhang, P. Effects of Extreme Thermal Shock on Microstructure and Mechanical Properties of Au-12Ge/Au/Ni/Cu Solder Joint. *Metals* **2020**, *10*, 1373. [CrossRef]

20. Dreyer, C.B.; Zacny, K.; Steele, J.P.; Schwendeman, J.R.; Paulsen, G.; Andersen, R.C.; Skok, J. Development of a thin section device for space exploration: Overview and system performance estimates. *Adv. Space Res.* **2013**, *51*, 1659–1673. [CrossRef]
21. Yu, Z.L.; Xin, R.L.; Xu, Z.Z.; Zhu, Y.N.; Zhang, X.L.; Hao, S.J.; Zhang, Z.H.; Liang, P. Investigation on the Mechanical Properties and Shape Memory Effect of Landing Buffer Structure Based on NiTi Alloy Printing. *Chin. J. Mech. Eng.* **2023**, *36*, 104. [CrossRef]
22. Singh, H.; Khosla, H.; Sidhu, T.S.; Kalsi, S.B.S.; Karthikeyan, J. Characteristic study of N07718 superalloy surface prepared by cold spray. *Mater. Manuf. Process.* **2017**, *33*, 140–148. [CrossRef]
23. Xu, K.; Yin, Y.X.; Chen, C. Research and application progress of welding technology under extreme conditions. *Arch. Civ. Mech. Eng.* **2024**, *24*, 182. [CrossRef]
24. Tang, M.; Pistorius, P.C. Fatigue life prediction for $AlSi_{10}Mg$ components produced by selective laser melting. *Int. J. Fatigue* **2019**, *125*, 479–490. [CrossRef]
25. Wu, S.; Tang, Y.N.; Gu, J.; Li, R.T.; Liang, Y.; Liu, P.L.; Wang, H.X.; An, C.H.; Deng, Q.B.; Zhao, L.B.; et al. Controllable preparation of metal-based lubrication coatings in extreme environmental applications. *Mater. Des.* **2024**, *241*, 112922. [CrossRef]
26. Xiao, J.; Zhang, H.Y.; Gong, S.K.; Xu, H.B.; Guo, H.B. High-temperature oxidation resistance of Si-coated C/SiC composites. *Rare Met.* **2024**, *43*, 4566–4572. [CrossRef]
27. Li, Z.W.; Gao, W.; Kwok, P.M.; Li, S.; He, Y.D. Electro-spark deposition coatings for high temperature oxidation resistance. *High Temp. Mater. Process.* **2000**, *19*, 443–458. [CrossRef]
28. Dudziak, T.; Datta, P.K.; Mayrhofer, P.H.; Rovere, F. High Temperature Oxidation Resistance of CrAlYN-Coated $Ti_{45}Al_8Nb$. *Oxid. Met.* **2011**, *75*, 359–376. [CrossRef]
29. Ouyang, T.Y.; Fang, X.W.; Zhang, Y.; Liu, D.W.; Wang, Y.; Feng, S.J.; Zhou, T.; Cai, S.Z.; Suo, J.P. Enhancement of high temperature oxidation resistance and spallation resistance of SiC-self-healing thermal barrier coatings. *Surf. Coat. Technol.* **2016**, *286*, 365–375. [CrossRef]
30. Feng, Y.; Dong, T.S.; Li, G.L.; Wang, R.; Zhao, X.W.; Liu, Q. High temperature oxidation resistance and TGO growth mechanism of laser remelted thermal barrier coatings. *J. Alloys Compd.* **2020**, *828*, 154266. [CrossRef]
31. Zhang, Y.F.; Jiang, H.T.; Tian, S.W.; Xu, W.; Wang, T.X.; Zhang, S.Y.; Zeng, S.W.; Luo, W.; Zhang, Y. High temperature oxidation resistance of TNM alloy coated with/without 8YSZ/NiCoCrAlY thermal barrier coatings. *Appl. Surf. Sci.* **2023**, *611*, 155704. [CrossRef]
32. Romero, R.; Domínguez, A.; López-Escalante, M.; Martín, F.; Romero-Gomez, P.; Palanco, S.; Leinen, D. Silver zirconium oxide cermet coatings spray deposited onto galvanized steel sheet for low temperature solar applications. *Ceram. Int.* **2023**, *49*, 33643–33651. [CrossRef]
33. Choi, J.J.; Choi, J.H.; Park, D.S. Application of Low Temperature Ceramic Coating Process for SOFC Electrolyte and Electrode Fabrication. *ECS Trans.* **2013**, *57*, 657. [CrossRef]
34. Jiang, K.; Qu, Y.D.; You, J.H.; Li, R.D.; Xiang, Q.C.; Zhou, Y.X. Influence of Cr element on impact fracture process of ductile Ni-resistant alloyed iron at low temperature. *China Foundry* **2016**, *13*, 42–46. [CrossRef]
35. Ekabote, N.; Kodancha, K.G.; Khan, T.M.Y.; Badruddin, I.A. Effect of Strain Rate and Temperature on Tensile and Fracture Performance of AA2050-T84 Alloy. *Materials* **2022**, *15*, 1590. [CrossRef] [PubMed]
36. Li, X.J.; Zhang, H.; Sha, J.B. Effect of Vacuum Induction Melting Technology on Mechanical Properties of Nb-16Si-22Ti-2Al-2Hf-17Cr Alloy. *Int. J. Mod. Phys. B* **2010**, *24*, 2940–2945. [CrossRef]
37. Nedashkovskii, K.I.; Zheleznyak, O.N.; Gromyko, B.M.; Kozykov, B.A.; Mikhalev, I.A. Effect of low temperatures on Mechanical and physical properties of high-strength nickel alloy ÉK61-ID and stainless maraging steel ÉK49-VD. *Met. Sci. Heat Treat.* **2003**, *45*, 233–236. [CrossRef]
38. Liu, D.K.; Yang, J.; Zhang, Y.H. Toughness and fracture mechanism at low temperature of offshore engineering steel at different welding heat inputs. *Metall. Res. Technol.* **2022**, *119*, 405. [CrossRef]
39. Yao, C.G.; Lv, H.J.; Yi, D.Q.; Meng, S.; Xiao, L.R.; Wang, B. Microstructures and Mechanical Properties of Inconel 718 Alloy at Ultralow Temperatures. *J. Mater. Eng. Perform.* **2018**, *27*, 2060–2069. [CrossRef]
40. Rao, B.C.; Srinivas, M.; Kamat, S. Effect of temperature on fracture toughness of Timetal 834 titanium alloy under mode I and mixed mode I-III loading. *Met. Mater. Trans. A* **2008**, *39*, 1340–1349. [CrossRef]
41. Clinton, J.A.; Morrison, R.L.; Carter, J.L.W. Effects of Changes in Test Temperature on Tensile Properties and Notched *Vs* Fatigue Precracked Toughness of a Zr-Based BMG Composite. *Metall. Mater. Trans. A* **2017**, *48*, 3220–3230. [CrossRef]
42. Qu, W.Q.; Song, M.Y.; Yao, J.S.; Zhao, H.Y. Effect of temperature and heat treatment status on the ductile fracture toughness of 2219 aluminum alloy. In *Materials Modeling, Simulation, and Characterization*; Trans Tech Publications: Zurich, Switzerland, 2011.
43. Li, D.; Meng, Z.C.; Shen, Y.Y.; Zhang, J.H.; Hu, M.; Qiu, J.K.; Li, S.J. Study of low-temperature impact deformation behavior of Ti-6Al-4V alloy. *Vacuum* **2024**, *222*, 113066. [CrossRef]
44. Srinivasan, V.S.; Ibanez, A.R.; Saxena, A. Modeling of creep crack growth and fracture toughness behaviour of directionally solidified GTD 111 superalloy. *Trans. Indian Inst. Met.* **2010**, *63*, 453–456. [CrossRef]

45. Zhang, F.; Qian, K.; Lu, P.; Liu, S.; Lu, S.; Liu, Q.; Cui, B. Quasi-static compressive fracture behavior of three-period minimum surface Al_2O_3/Al composites fabricated by stereolithography. *J. Mater. Res. Technol.* **2024**, *30*, 4950–4960. [CrossRef]
46. Wu, Y.S.; Qin, X.Z.; Wang, C.S.; Zhou, L.Z. Microstructural evolution and its influence on the impact toughness of GH984G alloy during long-term thermal exposure. *J. Mater. Sci. Technol.* **2021**, *60*, 61–69. [CrossRef]
47. Tsuchida, Y.; Inoue, T.; Suzuki, T. Creep rupture strength of V-modified 2 1/4Cr-1Mo steel. *Int. J. Press. Vessel. Pip.* **2004**, *81*, 191–197. [CrossRef]
48. Jiang, T.; Chen, L.B.; Jiang, F.; Cai, H.P.; Sun, J. Microstructural evolution and mechanical properties of a nickel-based superalloy through long-term service. *Mater. Sci. Eng. A* **2016**, *656*, 184–189. [CrossRef]
49. Li, H.F.; Ye, F.; Zhao, J.; Cao, T.S.; Xu, F.H.; Xu, Q.S.; Wang, Y.; Cheng, C.Q.; Min, X.H. Grain boundary migration-induced directional coarsening of the γ' phase in advanced ultra-supercritical superalloy. *Mater. Sci. Eng. A* **2018**, *714*, 172–178. [CrossRef]
50. van Dalen, M.E.; Seidman, D.N.; Dunand, D.C. Creep- and coarsening properties of Al-0.06 at.% Sc-0.06 at.% Ti at 300–450 °C. *Acta Mater.* **2008**, *56*, 4369–4377. [CrossRef]
51. Angella, G.; Donnini, R.; Ripamonti, D.; Maldini, M. The role of particle ripening on the creep acceleration of Nimonic 263 superalloy. In Proceedings of the Eurosuperalloys 2014—2nd European Symposium on Superalloys and Their Applications, Giens, France, 12–16 May 2014.
52. Li, G.S.; Fang, M.; Xu, G.S.; Sun, R.; Chen, C.H.; Zhang, M.Y.; Li, J.H. Effect of high-temperature ECAP on grain coarsening and refinement. *Mater. Sci. Technol.* **2022**, *38*, 181–190. [CrossRef]
53. Qian, W.; Kai, X.Z.; Tao, R.; Cao, R.; Chen, G.; Zhao, Y.T. Microstructure evolution and high-temperature performances of AA6111 alloy strengthened by Sc, Zr co-microalloying. *Mater. Sci. Eng. A* **2023**, *887*, 145788. [CrossRef]
54. Cao, B.X.; Zhao, Y.L.; Yang, T.; Liu, C.T. $L1_2$-Strengthened Co-Rich Alloys for High-Temperature Structural Applications: A Critical Review. *Adv. Eng. Mater.* **2021**, *23*, 2100453. [CrossRef]
55. Liu, J.T.; Liu, S.W.; Zheng, H.L.; Huang, W.J.; Zhao, W.; Liao, W.B. Effects of Transient Thermal Shock on the Microstructure and Mechanical Properties of CoCrFeNiMn High-Entropy Alloy Coatings. *Front. Mater.* **2021**, *8*, 805296. [CrossRef]
56. Li, W.Y.; Wang, M.L.; Wang, X.D.; Wang, T.M.; Li, T.J.; Lu, Y.P. A novel Co-free high-entropy alloy with excellent antimicrobial and mechanical properties. *Rare Met.* **2024**, *44*, 581–590. [CrossRef]
57. Aizenshtein, M.; Ungarish, Z.; Woller, K.B.; Hayun, S.; Short, M.P. Mechanical and microstructural response of the $Al_{0.5}$CoCrFeNi high entropy alloy to Si and Ni ion irradiation. *Nucl. Mater. Energy* **2020**, *25*, 100813. [CrossRef]
58. Almisned, G.; Güler, Ö.; Özkul, I.; Baykal, D.S.; Alkarrani, H.; Kilic, G.; Mesbahi, A.; Tekin, H.O. Exploring thermodynamic, physical and radiative interaction properties of quinary FeNiCoCr high entropy alloys (HEAs): A multi-directional characterization study. *Phys. Scr.* **2024**, *99*, 115303. [CrossRef]
59. Meng, J.; Qiao, Y.; Chen, Y.; Liu, T.W.; Li, T.; Wang, H.Y.; Dai, L.H. A high-entropy alloy syntactic foam with exceptional cryogenic and dynamic properties. *Mater. Sci. Eng. A* **2023**, *876*, 145146. [CrossRef]
60. Gao, X.Y.; Liu, J.; Fu, W.J.; Huang, Y.J.; Ning, Z.L.; Zhang, Z.X.; Sun, J.F.; Chen, W. Strong and ductile CoCrFeNi high-entropy alloy microfibers at ambient and cryogenic temperatures. *Mater. Des.* **2023**, *233*, 112250. [CrossRef]
61. Yusenko, K.V.; Riva, S.; Crichton, W.A.; Spektor, K.; Bykova, E.; Pakhomova, A.; Tudball, A.; Kupenko, I.; Rohrbach, A.; Klemme, S.; et al. High-pressure high-temperature tailoring of High Entropy Alloys for extreme environments. *J. Alloys Compd.* **2018**, *738*, 491–500. [CrossRef]
62. Sonal, S.; Lee, J.H.Y. Recent Advances in Additive Manufacturing of High Entropy Alloys and Their Nuclear and Wear-Resistant Applications. *Metals* **2021**, *11*, 1980. [CrossRef]
63. Kong, F.L.; Inoue, A.; Wang, F.; Chang, C.T. The Influence of Boron and Carbon Addition on the Glass Formation and Mechanical Properties of High Entropy (Fe, Co, Ni, Cr, Mo)-(B, C) Glassy Alloys. *Coatings* **2024**, *14*, 118. [CrossRef]
64. Sfikas, A.K.; Kamnis, S.; Tse MC, H.; Christofidou, K.A.; Gonzalez, S.; Karantzalis, A.E.; Georgatis, E. Microstructural Evaluation of Thermal-Sprayed CoCrFeMnNi$_{0.8}$V High-Entropy Alloy Coatings. *Coatings* **2023**, *13*, 1004. [CrossRef]
65. Shi, Y.Z.; Li, R.; Lei, Z.F. Influences of Synthetic Parameters on Morphology and Growth of High Entropy Oxide Nanotube Arrays. *Coatings* **2023**, *13*, 46. [CrossRef]
66. Li, S.H.; Ni, X.D.; Tian, F.Y. *Ab Initio* Predicted Alloying Effects on the Elastic Properties of Al_xHf_{1-x}NbTaTiZr High Entropy Alloys. *Coatings* **2015**, *5*, 366–377. [CrossRef]
67. Cui, K.X.; Zhang, Y. High-Entropy Alloy Films. *Coatings* **2023**, *13*, 635. [CrossRef]
68. Fan, R.; Zhao, S.C.; Wang, L.P.; Wang, L.; Guo, E.R. Effect of Annealing Temperature on the Microstructure and Mechanical Properties of CoCrFeNiNb$_{0.2}$Mo$_{0.2}$ High Entropy Alloy. *Materials* **2023**, *16*, 3987. [CrossRef] [PubMed]
69. Dufanets, M.; Sklyarchuk, V.; Plevachuk, Y.; Kulyk, Y.; Mudry, S. The Structural and Thermodynamic Analysis of Phase Formation Processes in Equiatomic AlCoCuFeNiCr High-Entropy Alloys. *J. Mater. Eng. Perform.* **2020**, *29*, 7321–7327. [CrossRef]
70. Gao, Y.; Bai, S.S.; Chong, K.; Liu, C.; Cao, Y.W.; Zou, Y. Machine learning accelerated design of non-equiatomic refractory high entropy alloys based on first principles calculation. *Vacuum* **2023**, *207*, 111608. [CrossRef]

71. Kwon, Y.J.; Won, Y.J.; Cho, K.S. Thermodynamic evaluation of the phase stability in mechanically alloyed AlCuxNiCoTi high-entropy alloys. *J. Alloys Compd.* **2023**, *948*, 169772. [CrossRef]
72. Hsu, U.S.; Hung, U.D.; Yeh, J.W.; Chen, S.K.; Huang, Y.S.; Yang, C.C. Alloying behavior of iron, gold and silver in AlCoCrCuNi-based equimolar high-entropy alloys. *Mater. Sci. Eng. A* **2007**, *460*, 403–408. [CrossRef]
73. Feng, L.; Qin, G.; Yang, X.; Ren, H.; Chen, R.R. Influence of aging heat treatment on the microstructure and mechanical properties of $Co_{29}Cr_{31}Cu_4Mn_{15}Ni_{21}$ high-entropy alloys strengthened by nano-precipitates. *Mater. Sci. Eng. A* **2025**, *920*, 147508. [CrossRef]
74. Hsu W., L.; Tsai C., W.; Yeh A., C.; Yeh J., W. Clarifying the four core effects of high-entropy materials. *Chin. Sci. Bull.-Chin Nat. Rev. Chem.* **2024**, *8*, 471–485. [CrossRef]
75. Wang, Q.; Yang, W.C.; Lin, S.S.; Liu, C.; Qin, J.R.; Qu, P.F.; Zhang, J.; Liu, L. A novel L12-strengthened single crystal high entropy alloy with excellent high-temperature mechanical properties. *Mater. Charact.* **2024**, *212*, 113958. [CrossRef]
76. Li, A.; Kang, K.; Yu, S.; Zhang, J.; Xu, M.; Huang, D.; Che, C.; Liu, S.; Jiang, Y.; Li, G. Heterogeneous structure and dual precipitates induced excellent strength-ductility combination in $CoCrNiTi_{0.1}$ medium entropy alloy. *Mater. Sci. Eng. A* **2024**, *912*, 146992. [CrossRef]
77. Jiang, F.; Wang, J.R.; Jiang, Q.W.; Yang, G.J.; Xu, M.Q.; Xu, W.Q.; Tang, C.G.; Yi, J.J. An excellent synergy in yield strength and plasticity of $NbTiZrTa_{0.25}Cr_{0.4}$ refractory high entropy alloy through the regulation of cooling rates. *Int. J. Refract. Met. Hard Mater.* **2023**, *117*, 106409. [CrossRef]
78. Li, H.G.; Huang, Y.J.; Sun, J.F.; Lu, Y.Z. The relationship between thermo-mechanical history, microstructure and mechanical properties in additively manufactured CoCrFeMnNi high entropy alloy. *J. Mater. Sci. Technol.* **2021**, *77*, 187–195. [CrossRef]
79. Fan, R.; Guo, E.J.; Wang, L.P.; Wang, L.; Zhao, S.C.; Li, X.M.; Zhang, X.; Cui, B. Multi-scale microstructure strengthening strategy in $CoCrFeNiNb_{0.1}Mo_{0.3}$ high entropy alloy overcoming strength-ductility trade-off. *Mater. Sci. Eng. A* **2023**, *882*, 145446. [CrossRef]
80. Feng, R.; Rao, Y.; Liu, C.H.; Xie, X.; Yu, D.J.; Chen, Y.; Ghazisaeidi, M.; Ungar, T.; Wang, H.M.; An, K.; et al. Enhancing fatigue life by ductile-transformable multicomponent B2 precipitates in a high-entropy alloy. *Nat. Commun.* **2021**, *12*, 3588. [CrossRef] [PubMed]
81. Tunes, M.; Vo, H.; Baldwin, J.; Saleh, T.; Fensin, S.; El-Atwani, O. Perspectives on novel refractory amorphous high-entropy alloys in extreme environments. *Appl. Mater. Today* **2023**, *32*, 101796. [CrossRef]
82. Barron, P.; Carruthers, A.; Fellowes, J.; Jones, N.; Dawson, H.; Pickering, E. Towards V-based high-entropy alloys for nuclear fusion applications. *Scr. Mater.* **2019**, *176*, 12–16. [CrossRef]
83. Lang, E.; Burns, K.; Wang, Y.; Kotula, P.G.; Kustas, A.B.; Rodriguez, S.; Aitkaliyeva, A.; Hattar, K. Compositional Effects of Additively Manufactured Refractory High-Entropy Alloys under High-Energy Helium Irradiation. *Nanomaterials* **2022**, *12*, 2014. [CrossRef]
84. Ward, T.Z.; Wilkerson, R.P.; Musicó, B.L.; Foley, A.; Brahlek, M.; Weber, W.J.; Sickafus, K.E.; Mazza, A.R. High entropy ceramics for applications in extreme environments. *J. Phys. Mater.* **2024**, *7*, 021001. [CrossRef]
85. El Atwani, O.; Vo, H.T.; Tunes, M.A.; Lee, C.; Alvarado, A.; Krienke, N.; Poplawsky, J.D.; Kohnert, A.A.; Gigax, J.; Chen, W.-Y.; et al. A quinary WTaCrVHf nanocrystalline refractory high-entropy alloy withholding extreme irradiation environments. *Nat. Commun.* **2023**, *14*, 2516. [CrossRef]
86. Yeh, J.W.; Chen, S.K.; Lin, S.J.; Gan, J.Y.; Chin, T.S.; Shun, T.T.; Tsau, C.H.; Chang, S.Y. Nanostructured high-entropy alloys with multiple principal elements: Novel alloy design concepts and outcomes. *Adv. Eng. Mater.* **2004**, *6*, 299–303. [CrossRef]
87. Cantor, B.; Chang IT, H.; Knight, P.; Vincent, A.J.B. Microstructural development in equiatomic multicomponent alloys. *Mater. Sci. Eng. A* **2004**, *375–377*, 213–218. [CrossRef]
88. Chen, J.; Zhou, X.Y.; Wang, W.L.; Liu, B.; Lv, Y.K.; Yang, W.; Xu, D.P.; Liu, Y. A review on fundamental of high entropy alloys with promising high-temperature properties. *J. Alloys Compd.* **2018**, *760*, 15–30. [CrossRef]
89. Cantor, B. Multicomponent and High Entropy Alloys. *Entropy* **2014**, *16*, 4749–4768. [CrossRef]
90. Zhang, Y.; Zuo, T.T.; Tang, Z.; Gao, M.C.; Dahmen, K.A.; Liaw, P.K.; Lu, Z.P. Microstructures and properties of high-entropy alloys. *Prog. Mater. Sci.* **2014**, *61*, 1–93. [CrossRef]
91. Lin, Y.P.; Yang, T.F.; Lang, L.; Shan, C.; Deng, H.Q.; Hu, W.Y.; Gao, F. Enhanced radiation tolerance of the Ni-Co-Cr-Fe high-entropy alloy as revealed from primary damage. *Acta Mater.* **2020**, *196*, 133–143. [CrossRef]
92. Kumar Napk Li, C.; Leonard, K.J.; Bei, H.; Zinkle, S.J. Microstructural stability and mechanical behavior of FeNiMnCr high entropy alloy under ion irradiation. *Acta Mater.* **2016**, *113*, 230–244. [CrossRef]
93. Nie, S.J.; Yi, X.N.; Zhou, H.L.; Zhu, H.J.; Yang, L.L.; Fu, F.L.; Li, J.Y.; Yang, H.K.; Xu, G.X.; Lu, S.; et al. Corrosion behavior of as-cast $Al_{0.75}CoFeCr_{1.25}Ni$ high entropy alloy in 0.5 mol/L NaOH solution. *J. Iron Steel Res. Int.* **2024**, *31*, 2852–2863. [CrossRef]
94. Huang, S.S.; Zhang, J.; Fu, H.J.; Xiong, Y.X.; Ma, S.H.; Xiang, X.P.; Xu, B.; Lu, W.Y.; Zhang, Y.W.; Weber, W.J.; et al. Irradiation performance of high entropy ceramics: A comprehensive comparison with conventional ceramics and high entropy alloys. *Prog. Mater. Sci.* **2024**, *143*, 101250. [CrossRef]
95. Zhang, Y.; Wang, Z.N.; Huang, S.Y.; Liu, H.; Yan, Y. Electrochemical behavior and passivation film characterization of TiZrHfNb multi-principal element alloys in NaCl-containing solution. *Corros. Sci.* **2024**, *235*, 112185. [CrossRef]

96. Zhong, M.X.; Xu, T.T.; Wang CX, Z.; Teng, Y.; Cai, Y.C.; Zhang, Z.W.; Xiao, B.; Wang, X. Utilizing high entropy oxide ($Ni_{0.2}Co_{0.2}Ca_{0.2}Cu_{0.2}Mg_{0.2}$)Fe 2 O 4 in chemical looping process for highly efficient and stable hydrogen production. *Chem. Eng. J.* **2024**, *487*, 150521. [CrossRef]
97. Kumar, A.; Abu Shaz, M.; Mukhopadhyay, N.K.; Yadav, T.P. Phase transformation of AB 5 to AB 2 type phase on substitution of Mn with Zr in TiVCoNi (Zr_xMn_{2-x}) (x = 0, 0.3, 0.6, 1.0) high entropy alloys. *Mater. Chem. Phys.* **2024**, *318*, 129291. [CrossRef]
98. Cui, X.Y.; Liu, Y.C.; Wang, X.Y.; Tian, X.L.; Wang, Y.X.; Zhang, G.; Liu, T.; Ding, J.; Hu, W.B.; Chen, Y.N. Rapid High-Temperature Liquid Shock Synthesis of High-Entropy Alloys for Hydrogen Evolution Reaction. *Acs Nano* **2024**, *18*, 2948–2957. [CrossRef] [PubMed]
99. Ren, J.T.; Chen, L.; Wang, H.Y.; Yuan, Z.Y. Non-precious metal high-entropy alloys with d-d electron interactions for efficient and robust hydrogen oxidation reactions in alkaline media. *Inorg. Chem. Front.* **2024**, *11*, 2029–2038. [CrossRef]
100. Liu, G.Y.; Yao, R.Y.; You, J.H.; Liu, L.L.; Yi, B.L.; Zhao, Y.; Li, Y.H.; Zhang, H.Z. Non-precious metal high-entropy electrocatalysts ($Al_{0.5}$NiCoCr-$X_{0.5}$) for OER application. *Mater. Today Commun.* **2024**, *39*, 109052. [CrossRef]
101. Ma, Y.J.; Ren, Y.L.; Sun, D.Y.; Wang, B.; Wu, H.; Bian, H.F.; Cao, J.D.; Cao, X.Y.; Ding, F.; Lu, J.H.; et al. High entropy alloy nanoparticles dual-decorated with nitrogen-doped carbon and carbon nanotubes as promising electrocatalysts for lithium-sulfur batteries. *J. Mater. Sci. Technol.* **2024**, *188*, 98–104. [CrossRef]
102. Zhang, C.; Zhao, Z.; Lin, X.; Wang, S.; Wang, J.; Li, Y.; Li, Y.; Zhang, Y.; Zhao, H. Molybdenum-14Rhenium Alloy—The Most Promising Candidate for High-Temperature Semiconductor Substrate Materials. *J. Alloys Compd.* **2024**, *991*, 174391. [CrossRef]
103. Wu, C.S.; Tsai, P.H.; Kuo, C.M.; Tsai, C.W. Effect of Atomic Size Difference on the Microstructure and Mechanical Properties of High-Entropy Alloys. *Entropy* **2018**, *20*, 967. [CrossRef]
104. Zhang, Y.; Zhou, Y. Solid solution formation criteria for high entropy alloys. In Proceedings of the PRICM 6: Sixth Pacific Rim International Conference on Advanced Materials and Processing, Jeju Island, Republic of Korea, 5–9 November 2007.
105. Kube, S.A.; Sohn, S.; Uhl, D.; Datye, A.; Mehta, A.; Schroers, J. Phase selection motifs in High Entropy Alloys revealed through combinatorial methods: Large atomic size difference favors BCC over FCC. *Acta Mater.* **2019**, *166*, 677–686. [CrossRef]
106. Guo, S.; Liu, C.T. Phase stability in high entropy alloys: Formation of solid-solution phase or amorphous phase. *Prog. Nat. Sci.-Mater. Int.* **2011**, *21*, 433–446. [CrossRef]
107. Abu-Odeh, A.; Galvan, E.; Kirk, T.; Mao, H.; Chen, Q.; Mason, P.; Malak, R.; Arróyave, R. Efficient exploration of the High Entropy Alloy composition-phase space. *Acta Mater.* **2018**, *152*, 41–57. [CrossRef]
108. Tripathy, S.; Gupta, G.; Chowdhury, S.G. High Entropy Alloys: Criteria for Stable Structure. *Metall. Mater. Trans. A* **2018**, *49*, 7–17. [CrossRef]
109. Nong, Z.S.; Zhu, J.C.; Cao, Y.; Yang, X.W.; Lai, Z.H.; Liu, Y. Stability and structure prediction of cubic phase in as cast high entropy alloys. *Mater. Sci. Technol.* **2014**, *30*, 363–369. [CrossRef]
110. Niitsu, K.; Asakura, M.; Yuge, K.; Inui, H. Prediction of Face-Centered Cubic Single-Phase Formation for Non-Equiatomic Cr-Mn-Fe-Co-Ni High-Entropy Alloys Using Valence Electron Concentration and Mean-Square Atomic Displacement. *Mater. Trans.* **2020**, *61*, 1874–1880. [CrossRef]
111. Trung, T.B.; Phuong, D.D.; Toan, N.V.; Linh, N.N.; Bach, T.N.; Bures, R. Soft Magnetic and Mechanical Properties of FeNiCoSi$_{0.25}$Al$_x$ (x = 0-1) High Entropy Alloys Prepared by Arc Melting. *Mater. Trans.* **2021**, *62*, 1597–1603. [CrossRef]
112. Yu, Y.; Wang, J.; Li, J.S.; Kou, H.C.; Li, W.M. Characterization of BCC phases in AlCoCrFeNiTiχ high entropy alloys. *Mater. Lett.* **2015**, *138*, 78–80. [CrossRef]
113. Zhang, L.; Zhou, D.; Li, B.S. Anomalous microstructure and excellent mechanical properties of $Ni_{35}Al_{21.67}Cr_{21.67}Fe_{21.67}$ high-entropy alloy with BCC and B2 structure. *Mater. Lett.* **2018**, *216*, 252–255. [CrossRef]
114. Zhang, Z.; Li, J.N.; Fan, Z.Y.; Ye, Z.Y.; Li, Y.J.; Zhang, C.Y.; Jing, C.N. Microstructures and corrosion resistance enhancement of ultrasonic vibration-assisted medium entropy alloy base laser multi-phase coating. *Surf. Coat. Technol.* **2023**, *454*, 129144. [CrossRef]
115. Shen, X.; Sun, B.R.; Xin, S.W.; Ding, S.J.; Shen, T.D. Creep in a nanocrystalline VNbMoTaW refractory high-entropy alloy. *J. Mater. Sci. Technol.* **2024**, *187*, 221–229. [CrossRef]
116. El-Atwani, O.; Alvarado, A.; Unal, K.; Fensin, S.; Hinks, J.; Greaves, G.; Baldwin, J.; Maloy, S.; Martinez, E. Helium implantation damage resistance in nanocrystalline W-Ta-V-Cr high entropy alloys. *Mater. Today Energy* **2020**, *19*, 100599. [CrossRef]
117. Luan, H.-W.; Shao, Y.; Li, J.-F.; Mao, W.-L.; Han, Z.-D.; Shao, C.; Yao, K.-F. Phase stabilities of high entropy alloys. *Scr. Mater.* **2020**, *179*, 40–44. [CrossRef]
118. Kim, Y.S.; Chae, H.; Huang, E.W.; Jain, J.; Harjo, S.; Kawasaki, T.; Hong, S.I.; Lee, S.Y. Microstructural Evolution and Mechanical Properties of Non-Equiatomic $(CoNi)_{74.66}Cr_{17}Fe_8C_{0.34}$ High-Entropy Alloy. *Materials* **2022**, *15*, 1312. [CrossRef] [PubMed]
119. Xiong, F.; Tang, S.W.; Yan, J.H.; Fu, R.D. Tailoring the microstructure of a non-equiatomic $Fe_{40}Mn_{27}Ni_{26}Co_5Cr_2$ high-entropy alloy via friction stir processing. *J. Mater. Res. Technol.* **2024**, *31*, 1443–1449. [CrossRef]
120. Bridges, D.; Zhang, S.H.; Lang, S.; Gao, M.R.; Yu, Z.Z.; Feng, Z.L.; Hu, A.M. Laser brazing of a nickel-based superalloy using a Ni-Mn-Fe-Co-Cu high entropy alloy filler metal. *Mater. Lett.* **2018**, *215*, 11–14. [CrossRef]

121. Ishizu, N.; Kitagawa, J. New high-entropy alloy superconductor $Hf_{21}Nb_{25}Ti_{15}V_{15}Zr_{24}$. *Results Phys.* **2019**, *13*, 102275. [CrossRef]
122. Qin, F.; Dai, K.Q.; Chen, S.H.; Li, J.J. Nickel content-dependent microstructure and mechanical properties of TiZrNbHfNi high entropy alloy thin films. *Mater. Today Commun.* **2024**, *38*, 107932. [CrossRef]
123. Li, X.J.; Schonecker, S.; Li, X.Q.; Li, W.; Liang, X.Q.; Vitos, L. First-principles calculations of the cleavage energy in random solid solutions: A case study for TiZrNbHf high-entropy alloy. *Comput. Mater. Sci.* **2022**, *212*, 111575. [CrossRef]
124. Gabáni, S.; Cedervall, J.; Ek, G.; Pristáš, G.; Orendáč, M.; Bačkai, J.; Onufriienko, O.; Gažo, E.; Flachbart, K. Search for superconductivity in hydrides of TiZrNb, TiZrNbHf and TiZrNbHfTa equimolar alloys. *Phys. B Condens. Matter* **2022**, *648*, 414414. [CrossRef]
125. Qiao, J.W.; Ma, S.G.; Huang, E.W.; Chuang, C.P.; Liaw, P.K.; Zhang, Y. Microstructural Characteristics and Mechanical Behaviors of AlCoCrFeNi High-Entropy Alloys at Ambient and Cryogenic Temperatures. *Mater. Sci. Forum* **2011**, *688*, 419–425. [CrossRef]
126. Gali, A.; George, E.P. Tensile properties of high- and medium-entropy alloys. *Intermetallics* **2013**, *39*, 74–78. [CrossRef]
127. Bhattacharjee, T.; Zheng, R.X.; Chong, Y.; Sheikh, S.; Guo, S.; Clark, I.T.; Okawa, T.; Wani, I.S.; Bhattacharjee, P.P.; Shibata, A.; et al. Effect of low temperature on tensile properties of $AlCoCrFeNi_{2.1}$ eutectic high entropy alloy. *Mater. Chem. Phys.* **2018**, *210*, 207–212. [CrossRef]
128. Jaladurgam, N.R.; Lozinko, A.; Guo, S.; Harjo, S.; Colliander, M.H. Load redistribution in eutectic high entropy alloy $AlCoCrFeNi_{2.1}$ during high temperature deformation. *Materialia* **2022**, *22*, 101392. [CrossRef]
129. Tabachnikova, E.D.; Shapovalov, Y.O.; Smirnov, S.N.; Gorban, V.F.; Krapivka, N.A.; Firstov, S.A. Low-temperature mechanical properties and thermally activated plasticity parameters of the $CrMnFeCoNi_2Cu$ high entropy alloy. *Low Temp. Phys.* **2020**, *46*, 958–968. [CrossRef]
130. Semerenko, Y.O.; Natsik, V.D.; Tabachnikova, E.D.; Huang, Y.; Langdon, T.G. Mechanisms of Low-Temperature Dislocation Motion in High-Entropy $Al_{0.5}CoCrCuFeNi$ Alloy. *Metals* **2024**, *14*, 778. [CrossRef]
131. Bulatov, O.S.; Klochko, V.S.; Korniyets, A.V.; Kolodiy, I.V.; Kondratov, O.O.; Tikhonovska, T.M. Low temperature elastic properties of $Al_{0.5}CoCrCuFeNi$ high-entropy alloy. *Funct. Mater.* **2021**, *28*, 492–496.
132. Otto, F.; Dlouhý, A.; Somsen, C.; Bei, H.; Eggeler, G.; George, E.P. The influences of temperature and microstructure on the tensile properties of a CoCrFeMnNi high-entropy alloy. *Acta Mater.* **2013**, *61*, 5743–5755. [CrossRef]
133. Gludovatz, B.; Hohenwarter, A.; Catoor, D.; Chang, E.H.; George, E.P.; Ritchie, R.O. A fracture-resistant high-entropy alloy for cryogenic applications. *Science* **2014**, *345*, 1153–1158. [CrossRef]
134. Li, Z.; Zhao, S.; Diao, H.; Liaw, P.K.; Meyers, M.A. High-velocity deformation of Al0.3CoCrFeNi high-entropy alloy: Remarkable resistance to shear failure. *Sci. Rep.* **2017**, *7*, 42742. [CrossRef]
135. Kim, J.H.; Lim, K.R.; Won, J.W.; Na, Y.S.; Kim, H.S. Mechanical properties and deformation twinning behavior of as-cast CoCrFeMnNi high-entropy alloy at low and high temperatures. *Mater. Sci. Eng. A* **2018**, *712*, 108–113. [CrossRef]
136. Kireeva, I.; Chumlyakov, Y.; Vyrodova, A.; Pobedennaya, Z.; Karaman, I. Effect of twinning on the orientation dependence of mechanical behaviour and fracture in single crystals of the equiatomic CoCrFeMnNi high-entropy alloy at 77K. *Mater. Sci. Eng. A* **2020**, *784*, 139315. [CrossRef]
137. Yang, F.; Dong, L.; Cai, L.; Hu, X.; Fang, F. Mechanical properties of FeMnCoCr high entropy alloy alloyed with C/Si at low temperatures. *J. Alloys Compd.* **2021**, *859*, 157876. [CrossRef]
138. Rusakova, H.; Fomenko, L.; Smirnov, S.; Podolskiy, A.; Shapovalov, Y.; Tabachnikova, E.; Tikhonovsky, M.; Levenets, A.; Zehetbauer, M.; Schafler, E. Low temperature micromechanical properties of nanocrystalline CoCrFeNiMn high entropy alloy. *Mater. Sci. Eng. A* **2021**, *828*, 142116. [CrossRef]
139. Tan, Y.Y.; Chen, Z.J.; Su, M.Y.; Ding, G.; Jiang, M.Q.; Xie, Z.C.; Gong, Y.; Wu, T.; Wu, Z.-H.; Wang, H.-Y.; et al. Lattice distortion and magnetic property of high entropy alloys at low temperatures. *J. Mater. Sci. Technol.* **2022**, *104*, 236–243. [CrossRef]
140. Chaudhary, V.; Soni, V.; Gwalani, B.; Ramanujan, R.V.; Banerjee, R. Influence of non-magnetic Cu on enhancing the low temperature magnetic properties and Curie temperature of FeCoNiCrCu(x) high entropy alloys. *Scr. Mater.* **2020**, *182*, 99–103. [CrossRef]
141. Jiang, W.; Zhou, J.; Zhou, K.; Mao, Q.; Zhao, Y.; Meng, A.; Li, Z.; Li, J. Coupling effect of temperature and strain rate on mechanical properties and deformation mechanisms of $Cr_{26}Mn_{20}Fe_{20}Co_{20}Ni_{14}$ high-entropy alloy. *Mater. Sci. Eng. A* **2024**, *901*, 146525. [CrossRef]
142. Semerenko, Y.; Tabachnikova, E.; Hryhorova, T.; Shumilin, S.; Zoryansky, V. Low-Temperature Elastic Properties of Molybdenum Doped Non-Equiatomic High Entropy Alloys of the Fe-Co-Ni-Cr System. *Defect Diffus. Forum* **2024**, *431*, 55–59. [CrossRef]
143. Moon, J.; Tabachnikova, E.; Shumilin, S.; Hryhorova, T.; Estrin, Y.; Brechtl, J.; Liaw, P.K.; Wang, W.; Dahmen, K.A.; Zargaran, A.; et al. Deformation behavior of a Co-Cr-Fe-Ni-Mo medium-entropy alloy at extremely low temperatures. *Mater. Today* **2021**, *50*, 55–68. [CrossRef]
144. Wang, Q.; Amar, A.; Jiang, C.L.; Luan, H.W.; Zhao, S.F.; Zhang, H.; Le, G.M.; Liu, X.; Wang, X.Y.; Yang, X.S.; et al. $CoCrFeNiMo_{0.2}$ high entropy alloy by laser melting deposition: Prospective material for low temperature and corrosion resistant applications. *Intermetallics* **2020**, *119*, 106727. [CrossRef]

145. Wang, S.; Wu, M.; Shu, D.; Zhu, G.; Wang, D.; Sun, B. Mechanical instability and tensile properties of TiZrHfNbTa high entropy alloy at cryogenic temperatures. *Acta Mater.* **2020**, *201*, 517–527. [CrossRef]
146. Hu, M.L.; Song, W.D.; Duan, D.B.; Wu, Y. Dynamic behavior and microstructure characterization of TaNbHfZrTi high-entropy alloy at a wide range of strain rates and temperatures. *Int. J. Mech. Sci.* **2020**, *182*, 105738. [CrossRef]
147. Jo, Y.H.; Choi, W.M.; Sohn, S.S.; Kim, H.S.; Lee, B.J.; Lee, S. Role of brittle sigma phase in cryogenic-temperature-strength improvement of non-equi-atomic Fe-rich VCrMnFeCoNi high entropy alloys. *Mater. Sci. Eng. A* **2018**, *724*, 403–410. [CrossRef]
148. Zhang, C.; Yu, Q.; Tang, Y.T.; Xu, M.; Wang, H.; Zhu, C.; Ell, J.; Zhao, S.; MacDonald, B.E.; Cao, P.; et al. Strong and ductile FeNiCoAl-based high-entropy alloys for cryogenic to elevated temperature multifunctional applications. *Acta Mater.* **2023**, *242*, 118449. [CrossRef]
149. Dixit, S.; Rodriguez, S.; Jones, M.R.; Buzby, P.; Dixit, R.; Argibay, N.; DelRio, F.W.; Lim, H.H.; Fleming, D. Refractory High-Entropy Alloy Coatings for High-Temperature Aerospace and Energy Applications. *J. Therm. Spray Technol.* **2022**, *31*, 1021–1031. [CrossRef]
150. Senkov, O.N.; Wilks, G.B.; Miracle, D.B.; Chuang, C.P.; Liaw, P.K. Refractory high-entropy alloys. *Intermetallics* **2010**, *18*, 1758–1765. [CrossRef]
151. Ghosh, S.; Patnamsetty, M.; Somani, M.C.; Peura, P. Characteristics of dynamic softening during high temperature deformation of CoCrFeMnNi high-entropy alloy and its correlation with the evolving microstructure and micro-texture. *J. Mater. Res. Technol.* **2021**, *15*, 6608–6623. [CrossRef]
152. Jiang, D.; Li, Z.; Xu, J.; Ren, Q.; Agbedor, S.O.; Lei, Q. High-temperature oxidation behaviors of an equiatomic CrMnFeCoNi high entropy alloy. *Mater. Today Commun.* **2022**, *32*, 104185. [CrossRef]
153. Joseph, J.; Senadeera, M.; Chao, Q.; Shamlaye, K.; Rana, S.; Gupta, S.; Venkatesh, S.; Hodgson, P.; Barnett, M.; Fabijanic, D. Computational design of thermally stable and precipitation-hardened Al-Co-Cr-Fe-Ni-Ti high entropy alloys. *J. Alloys Compd.* **2021**, *888*, 161496. [CrossRef]
154. Joseph, J.; Annasamy, M.; Kada, S.R.; Hodgson, P.D.; Barnett, M.R.; Fabijanic, D.M. Optimising the Al and Ti compositional window for the design of γ′ (L12)-strengthened Al–Co–Cr–Fe–Ni–Ti high entropy alloys. *Mater. Sci. Eng. A* **2022**, *835*, 142620. [CrossRef]
155. Zhang, L.; Zhou, Y.; Jin, X.; Du, X.; Li, B. The microstructure and high-temperature properties of novel nano precipitation-hardened face centered cubic high-entropy superalloys. *Scr. Mater.* **2018**, *146*, 226–230. [CrossRef]
156. Lim, K.R.; Lee, K.S.; Lee, J.S.; Kim, J.Y.; Chang, H.J.; Na, Y.S. Dual-phase high-entropy alloys for high-temperature structural applications. *J. Alloys Compd.* **2017**, *728*, 1235–1238. [CrossRef]
157. Ma, Q.; Zhang, H.; Lv, Y.; Song, C.; Guo, N.; Xiao, G.; Zhao, W. Microstructure and properties of $W_{0.5}Ta_{0.3}$MoNbVAlTi1-xZrx high entropy alloy coatings by laser cladding on the surface of 45# steel. *Ceram. Int.* **2023**, *49*, 36416–36428.
158. Wang, M.; Ma, Z.L.; Xu, Z.Q.; Cheng, X.W. Designing VxNbMoTa refractory high-entropy alloys with improved properties for high-temperature applications. *Scr. Mater.* **2021**, *191*, 131–136. [CrossRef]
159. Couzinié, J.P.; Heczko, M.; Mazánová, V.; Senkov, O.N.; Ghazisaeidi, M.; Banerjee, R.; Mills, M.J. High-temperature deformation mechanisms in a BCC+B2 refractory complex concentrated alloy. *Acta Mater.* **2022**, *233*, 117995. [CrossRef]
160. Liu, Z.; Shi, X.; Zhang, M.; Qiao, J. High-Temperature Mechanical Properties of $NbTaHfTiZrV_{0.5}$ Refractory High-Entropy Alloys. *Entropy* **2023**, *25*, 1124. [CrossRef] [PubMed]
161. Alvi, S.; Akhtar, F. High temperature tribology of CuMoTaWV high entropy alloy. *Wear* **2019**, *426*, 412–419. [CrossRef]
162. Jhong, M.J.; Jen, I.L.; Wang, K.K.; Yen, W.T.; Huang, J.C.; Jang JS, C.; Hsieh, K.-C.; Wu, H.J. Nano-structure to Laves phase: Reduced Thermal Conductivity from Medium-Entropy AlNbV to High-Entropy AlNbVCrTi Alloys. *Materialia* **2020**, *14*, 100889. [CrossRef]
163. He, F.; Wang, Z.J.; Cheng, P.; Wang, Q.; Li, J.J.; Dang, Y.Y.; Wang, J.C.; Liu, C.T. Designing eutectic high entropy alloys of $CoCrFeNiNb_X$. *J. Alloys Compd.* **2016**, *656*, 284–289. [CrossRef]
164. Pang, J.; Zhang, H.; Ji, Y.; Zhu, Z.; Zhang, L.; Li, H.; Li, H.; Wang, A.; Zhang, H. High-temperature structural and mechanical stability of refractory high-entropy alloy $Nb_{40}Ti_{25}Al_{15}V_{10}Ta_5Hf_3W_2$. *Mater. Charact.* **2023**, *205*, 113321. [CrossRef]
165. Qiu, Y.; Hu, Y.; Taylor, A.; Styles, M.; Marceau, R.; Ceguerra, A.; Gibson, M.; Liu, Z.; Fraser, H.; Birbilis, N. A lightweight single-phase AlTiVCr compositionally complex alloy. *Acta Mater.* **2017**, *123*, 115–124. [CrossRef]
166. Gorr, B.; Müller, F.; Azim, M.; Christ, H.J.; Müller, T.; Chen, H.; Kauffmann, A.; Heilmaier, M. High-Temperature Oxidation Behavior of Refractory High-Entropy Alloys: Effect of Alloy Composition. *Oxid. Met.* **2017**, *88*, 339–349. [CrossRef]
167. Shangguan, Z.; Ma, S.; Li, J.; Liu, P.; Wang, Z. Study on high-temperature oxidation of TiZrHfNbTaV high-entropy alloy. *Mater. Lett.* **2024**, *360*, 135907. [CrossRef]